A new kinetic scheme for Saint-Venant equations applied to debris avalanches

A. Mangeney-Castelnau, J.P. Vilotte, Marie-Odile Bristeau, François Bouchut, Benoît Perthame, C. Simeoni, S. Yernini

INRIA

INSTITUT NATIONAL DE RECHERCHE EN INFORMATIQUE ET EN AUTOMATIQUE

A new kinetic scheme for Saint-Venant equations applied to debris avalanches

A. Mangeney-Castelnau, J.P. Vilotte , M.O. Bristeau , F. Bouchut, B. Perthame, C. Simeoni ,

S. Yernini

N 4646

Novembre 2002

THME 4

ISSN 0249-6399 ISRN INRIA/RR--4646--FR+ENG

A new kinetic scheme for Saint-Venant equations applied to debris avalanches

A. Mangeney-Castelnau, J.P. Vilotte *, M.O. Bristeau †, F. Bouchut, B. Perthame, C. Simeoni ‡, S. Yernini §

Thème 4 — Simulation et optimisation
de systèmes complexes
Projet M3N

Rapport de recherche n° 4646 — Novembre 2002 — 34 pages

Abstract: Numerical modelling of debris avalanches is presented here. The model uses the long waves approximation, based on the small aspect ratio of debris avalanches, as in classical Saint-Venant models for shallow water. Depth-averaged equations using this approximation are derived in a reference frame linked to the topography. Debris avalanches are treated here as a dry granular flow with Coulomb-type behavior. The numerical finite volume method uses a kinetic scheme, based on the description of the microscopic behavior of the system, to define numerical fluxes at the interfaces of a finite element mesh. The main advantage of this method is to preserve the height positivity. The originality of the present scheme stands in the introduction of a Dirac distribution of particles at the microscopic scale, in order to describe the stopping of a granular mass when the driving forces are under the Coulomb threshold. Comparisons with analytical solutions for dam-break problems show the efficiency of the method to deal with significant discontinuities. The ability of the model to describe debris avalanche behavior is illustrated here by schematic 1D numerical simulations of an avalanche over simplified topography. Coulomb-type behavior with constant and variable friction angle are compared in the framework of this simple example. Numerical tests show that such approach does not only provide insights into the flowing and stopping stage of the granular mass but it also allows us to observe interesting behaviors, such as the existence of a fluidized zone behind a stopped granular mass in specific situations, suggesting the presence of horizontal surfaces in the deposited mass.

* Département de Modélisation Physique et Numérique, IPGP, F75252 - Paris Cedex 05 - France, e-mails: mangeney@ipgp.jussieu.fr, vilotte@ipgp.jussieu.fr

† INRIA Rocquencourt, M3N, e-mail: Marie-Odile.Bristeau@inria.fr

‡ Département de Mathématiques et Applications, ENS, 45, rue d'Ulm - 75230 Paris Cedex 05 - France, e-mails: Francois.Bouchut@ens.fr, Benoit.Perthame@ens.fr, Chiara.Simeoni@ens.fr

§ Center for Development of Advanced Computing, Pune University Campus, Ganesh Khind - Pune 411 007 - India, e-mail: sudhakar@cdac.ernet.in

Unit de recherche INRIA Rocquencourt
Domaine de Voluceau, Rocquencourt, BP 105, 78153 Le Chesnay Cedex (France)
Tlphone : +33 1 39 63 55 11 - Tlcopie : +33 1 39 63 53 30

Key-words: avalanche modelling, Coulomb friction, Saint-Venant equations, finite volume, kinetic scheme.

Un nouveau schéma cinétique pour les équations de Saint-Venant appliquées aux avalanches de débris

Résumé : Cette étude porte sur la modélisation numérique des avalanches de débris. Le modèle utilise l'approximation des ondes longues, basée sur le petit rapport d'aspect des avalanches de débris comme dans les modèles classiques de type Saint-Venant pour les eaux peu profondes. On dérive les équations moyennes sur la hauteur dans un référentiel lié à la topographie. On traite ici les avalanches de débris comme un écoulement granulaire sec avec comportement de type Coulomb.

La méthode de résolution numérique, de type volumes finis, utilise un schéma cinétique basé sur la description du comportement microscopique du système pour définir les flux numériques aux interfaces des cellules du maillage. Le principal avantage de cette méthode est de préserver la positivité de la hauteur de l'écoulement. L'originalité du schéma présenté ici réside dans l'introduction d'une distribution de Dirac de particules à l'échelle microscopique pour décrire l'arrêt de la masse granulaire quand les forces motrices sont sous le seuil de Coulomb.

Des comparaisons avec les solutions analytiques pour des problèmes de rupture de barrage montrent l'efficacité de la méthode pour traiter des discontinuités significatives. La capacité du modèle à décrire le comportement d'une avalanche de débris est illustrée par des simulations schématiques 1D sur une topographie simplifiée. Dans le cadre de cet exemple simple, on compare l'effet du frottement de type Coulomb avec angle de frottement variable ou non. Les résultats numériques montrent qu'une telle approche met en évidence non seulement les étapes d'écoulement et d'arrêt de la masse granulaire mais elle permet aussi, dans des situations particulières, d'observer des comportements intéressants tels que des zones fluidizées derrière une masse granulaire à l'arrêt, suggérant la présence de surfaces horizontales dans la masse déposée.

Mots-clés : Modélisation d'avalanches, frottement de Coulomb, équations de Saint-Venant, volumes finis, schéma cinétique

1 Introduction

Granular avalanches such as rock or debris flows regularly cause large amounts of human and material damages. The numerical simulation of granular avalanches should provide a useful tool for investigating, within realistic geological contexts, the dynamics of these flows and their arrest phase and for improving the risk assessment of such natural hazards. Computational models must however be able to correctly capture several features such as the formation of interacting surges [*Iverson*, 1997].

The physics and rheology of granular avalanches are indeed challenging problems and the subject of an active research [e.g. *Hunt*, 1994; *Laigle and Coussot*, 1997; *Arattano and Savage*, 1994; *Macedonio and Pareschi*, 1992; *Cheng-Lun et al.*, 1996; *Whipple*, 1997; *Iverson*, 1997]. Despite the lack of a clear physical understanding of avalanche flows, useful basic behaviors of granular avalanches can be derived from experimental approaches [e.g. *Pouliquen*, 1999; *Douady et al.*, 1999]. During a granular avalanche, the characteristic length in the flowing direction is generally much larger than the vertical one, i.e. the avalanche thickness. Such a long waves scaling argument has been widely used in the derivation of continuum flow models for granular avalanches [e.g. *Hunt*, 1985; *Iverson*, 1997, *Iverson and Denlinger*, 2001; *Jenkins*, 1999; *Jenkins et al.*, 1999; *Savage and Hutter*, 1989; *Hutter et al.*, 1995; *Harbitz*, 1998; *Douady et al.*, 1999]. This leads to depth-averaged models governed by generalized Saint-Venant equations. These models provide a fruitful paradigm for investigating the dynamics and the extent of granular avalanches in the presence of smooth topography [e.g. *Hutter et al.*, 1995; *Naaim et al.*, 1997; *Pouliquen*, 1999]. It is worth to mention that by construction these flow models do not address the problem of the initiation and destabilization phases of an avalanche, see *Aranson and Tsimring* [2001] for models describing these processes. Granular surface flow models are closely related to other Saint-Venant models used in ocean and hydraulic engineering to describe both wave propagation, hydraulic jumps and open channel flows among others.

Without going into detailed rheological assumptions, which would be rather uncertain due to the lack of a physical understanding of the actual forces acting in debris avalanches, it is of interest here to emphasize some of the characteristics that make such flows quite specific.

The first characteristic is that granular media have the ability to remain static (solid) even along an inclined surface. This observation is related by Coulomb to some macroscopic solid-like friction and the system is able to flow only when the driving force reaches a critical value. In classical Coulomb's friction, the friction coefficient remains constant [e.g. *Hutter et al.*, 1995; *Naaim et al.*, 1997]. More evolved friction models, which assume a friction coefficient that depends on both the avalanche mean velocity and thickness, has been recently proposed [e.g. *Pouliquen*, 1999; *Douady et al.*, 1999] based on laboratory experiments and theoretical assumptions. These models have been shown quite useful to explain the geometry of the flow in the presence of topography as well as the observed runout of granular avalanches. In both cases, the existence of a macroscopic friction threshold leads to nonsmooth dynamics that has to be handled within appropriate mathematical and numerical formulations.

The second characteristic is that topography along which the avalanche is flowing can be

quite steep and rough. Long waves approximation has therefore to be derived in a reference frame locally tangent to the bedrock or to the free surface of the flow, in contrast with the Galilean reference frame used in classical Saint-Venant models for hydraulic engineering. The definition of such a tangent frame of reference is not obvious for a realistic earth topography and is still a challenge problem. Strong variations of the bottom topography introduce a stiff source term in the governing flow equations, that strongly influences the properties of the models and leads to the occurrence of new steady states. When taking into account a Coulomb-type friction and a realistic bottom topography, the source term becomes not only stiff during the flow but also nonsmooth and shocks are expected to develop in finite time regardless of the initial conditions. These difficulties have long hindered the development of realistic models for debris avalanches.

Computational methods developed in geophysics for solving the governing conservation laws of debris avalanches have mostly focused on the resolution of shock waves and surges. They are often based on fractional step methods and high resolution approximate Riemann solvers, like the Harten-Lax-vanLeer (HLL) solver [e.g. *Toro*, 1997]. Most of these methods are based on conservative nonoscillatory finite differences [e.g. *Gray et al.*, 1999; *Wieland et al.*, 1999; *Tai*, 2000; *Tai et al.*, 2002] or finite volumes which have the nice property of being conservative with respect to the flow height [e.g. *Naaim et al.*, 1997; *Laigle and Coussot*, 1997; *Denlinger and Iverson*, 2001]. They are based on an Eulerian formulation, a Lagrangian formulation [e.g. *Zwinger*, 2000] or a Lagrangian-Eulerian operator splitting [e.g. *Mangeney et al.*, 2000]. Even though these Riemann methods present significant improvements over the early Lagrangian finite difference methods [e.g. *Savage and Hutter*, 1989, 1991; *Greve et al.*, 1994], they do not preserve height positivity. Specific numerical development has to be introduced in the wetting-drying transition, where the system loses hyperbolicity, and generally an artificial small height has to be introduced in the regions where no fluid is present (see *Heinrich et al.*, 2001).

We consider here an alternative numerical scheme to compute debris avalanches, based on the kinetic interpretation of the system. Kinetic schemes have been proposed by *Audusse et al.* [2000] and *Bristeau et al.* [2001] to compute Saint-Venant equations in hydraulic problems. A survey of the theoretical properties of these schemes can be found in *Perthame* [2002]. Recently, kinetic schemes have been extended to include stiff source terms [e.g. *Botchorishvilli et al.*, 2000; *Perthame and Simeoni*, 2001]. Kinetic schemes have been shown to preserve the height positivity and to be able to treat the wetting-drying transition. However, classical kinetic schemes do not allow liquid-solid transitions, associated with a nonsmooth friction. The idea of the present scheme is to introduce a "zero-temperature" kinetic approximation when the driving force is under the Coulomb threshold.

We first present the basic equations and the conservation laws which govern the evolution of granular avalanches along a realistic topography. In particular, by using classical scaling arguments for surface flows, we derive the depth-averaged Saint-Venant equations in a reference frame linked to the bed topography. Then we review some minimal assumptions, inspired from experiments, on the characteristics of the frictional behavior of granular avalanches. Then we present a numerical scheme based on a finite volume approximation

of the governing set of conservation laws. At this stage, we introduce a kinetic solver which takes into account the existence of a friction threshold. The accuracy of this kinetic scheme is assessed against the classical dam-break problem over an inclined plane. Finally, some of the potentialities of the kinetic scheme are illustrated by simulating a debris avalanche over a simple bed topography. Comparisons between models with constant and nonconstant friction are discussed based on the runout, the shape of the deposit and the mechanism of the stopping phase.

2 Equations

Debris avalanches are described here within a continuum theoretical framework, as an incompressible material with constant density [e.g. *Savage and Hutter*, 1989; *Iverson and Denlinger*, 2001]. The evolution is therefore governed at time $t \geq 0$ by the mass and momentum conservation laws,

$$\nabla \cdot \mathbf{u} = 0, \tag{2.1}$$

$$\rho \left(\frac{\partial \mathbf{u}}{\partial t} + \mathbf{u} \cdot \nabla \mathbf{u} \right) = -\nabla \cdot \sigma + \rho \mathbf{g}, \tag{2.2}$$

where $\mathbf{u}(x, y, z, t) = (u(x, y, z, t), v(x, y, z, t), w(x, y, z, t))$ denotes the three-dimensional velocity vector inside the avalanche in a (x, y, z)-coordinate system that will be discussed later, $\sigma(\mathbf{x}, \mathbf{y}, \mathbf{z}, \mathbf{t})$ is the Cauchy stress tensor, ρ is the mass density and $\mathbf{g}$ the gravitational acceleration. The bottom boundary, or bed, is described by a surface $\psi_b(x, y, z, t) = z - b(x, y) = 0$ and the free surface of the flow by $\psi_s(x, y, z, t) = z - s(x, y, t) = z - b(x, y) - h(x, y, t) = 0$, where $h(x, y, t)$ is the depth of avalanche layer.
A kinematic boundary condition is imposed on the free and bed surfaces, that specifies that mass neither enters nor leaves the free surface or the base,

$$\frac{\mathrm{d}\psi_s}{\mathrm{d}t}|_s = \left(\frac{\partial \psi_s}{\partial t} + \mathbf{u} \cdot \nabla \psi_{\mathbf{s}} \right) |_s = 0, \tag{2.3}$$

$$\frac{\mathrm{d}\psi_b}{\mathrm{d}t}|_b = \left(\frac{\partial \psi_b}{\partial t} + \mathbf{u} \cdot \nabla \psi_{\mathbf{b}} \right) |_b = 0, \tag{2.4}$$

as well as a stress free-boundary condition at the surface, neglecting the atmospheric pressure,

$$\sigma \cdot \mathbf{n_s} = \mathbf{0}, \tag{2.5}$$

where $\mathbf{n_s}$ denotes the unit vector normal to the free surface.

Depth-averaging of these equations and some shallow flow assumptions require the choice of an appropriate coordinate system. During the flow, the avalanche thickness is much smaller than its extent parallel to the bed. In the case of significant slopes, the shallow flow assumption is more significant in a reference frame linked to the topography and the classical shallow water approximation relating horizontal and vertical direction is not appropriate. As

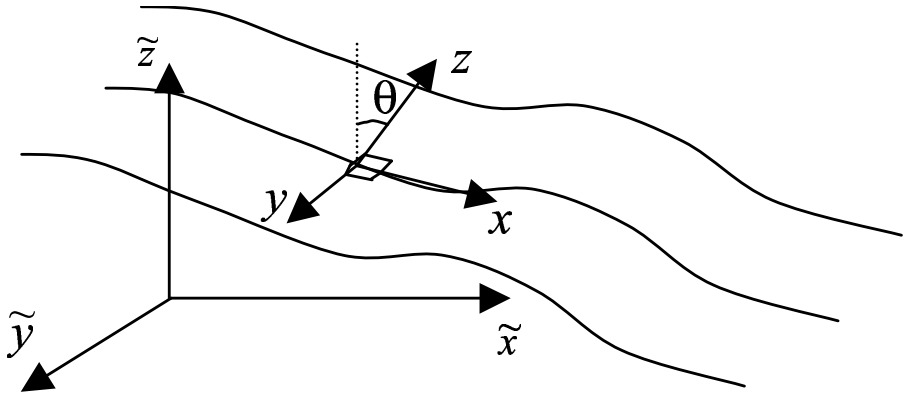

Figure 2.1: Reference frame (x, y, z) linked to the topography and Galilean reference frame $(\tilde{x}, \tilde{y}, \tilde{z})$ with θ the steepest slope angle.

in *Denlinger and Iverson* [2001], the equations are written here in terms of a local orthogonal Cartesian coordinate system in which the z-coordinate is normal to the local topography. We define a local x-axis corresponding to the projection of an arbitrary fixed $\tilde{x}$-direction in the local tangent plane to the topography and $\mathbf{y} = \mathbf{z} \wedge \mathbf{x}$ (Figure 2.1).
Note that the choice of an appropriate reference frame is not straightforward when dealing with real complex topography and may lead to nonorthonormal coordinate systems as in *Heinrich et al.* [2001], *Assier-Rzadkiewicz et al.* [2000] and *Sabot et al.* [1998]. The variation in space of a local coordinate system introduces errors in the calculation of the derivatives and require slow variation of the bedrock. The equations developed in a coordinate system linked to the topography are not directly applicable in a fixed reference frame as it was performed by *Naaim et al.* [1997] and *Naaim and Gurer* [1998]: appropriate rotations have to be used to transform properly topography-linked equations in a fixed reference frame [see *Douady et al.*, 1999].

In the reference frame linked to the topography (Figure 2.1), the equations of mass and momentum in the x- and y-direction, derived by integration of the Navier-Stokes equations (2.1)-(2.2) with boundary conditions (2.3)-(2.4) and (2.5), read

$$\frac{\partial h}{\partial t} + \mathrm{div}\,(h\bar{\mathbf{u}}) = 0, \tag{2.6}$$

$$\frac{\partial}{\partial t}(h\bar{u}) + \frac{\partial}{\partial x}(h\overline{u^2}) + \frac{\partial}{\partial y}(h\overline{uv}) = \gamma_x g h + \frac{1}{\rho}\frac{\partial}{\partial x}(h\overline{\sigma}_{xx}) + \frac{1}{\rho}\frac{\partial}{\partial y}(h\overline{\sigma}_{xy}) + \frac{1}{\rho}T_{tx}, \tag{2.7}$$

$$\frac{\partial}{\partial t}(h\bar{v}) + \frac{\partial}{\partial x}(h\overline{uv}) + \frac{\partial}{\partial y}(h\overline{v^2}) = \gamma_y g h + \frac{1}{\rho}\frac{\partial}{\partial x}(h\overline{\sigma}_{xy}) + \frac{1}{\rho}\frac{\partial}{\partial y}(h\overline{\sigma}_{yy}) + \frac{1}{\rho}T_{ty}, \tag{2.8}$$

where $\bar{\mathbf{u}} = (\bar{u}, \bar{v})$ denotes the depth-averaged horizontal flow velocity in the reference frame (x, y, z) defined below, h is the fluid depth, γ_i are coefficients (function of the local slope) defining the projection of the gravity vector along the i-direction and $T_{ti} = \sigma_{iz}|_b$ represents the traction at the base of the flow.
A small aspect ratio $\epsilon = H/L$, where H and L are characteristic dimensions along the z-axis and in the xOy plane respectively, is then introduced in the depth-averaged x- and y-equations (2.7)-(2.8) and in the nonaveraged z-equation obtained from the z-projection of equation (2.2). An asymptotic analysis with respect to ϵ [e.g. *Gray et al.*, 1999] leads to neglect the acceleration normal to the topography in the z-equation, leading to

$$\sigma_{zz} = \rho g \gamma_z \, (h - z) \, , \tag{2.9}$$

where $\gamma_z = \cos\theta$, with θ defined as the angle between the vertical axis and the normal to the topography (Figure 2.1). The shape of the vertical profile of the horizontal velocity in debris avalanche flows is still an open question. The conservation of the initial stratigraphy, sometimes observed in the deposits of a debris avalanche, has led to the assumption that all the deformation is essentially located in a fine boundary layer near the bed surface, so that the horizontal velocity is approximately constant over the depth [e.g. *Savage and Hutter*, 1989; *Naaim et al.*, 1997]. More recently, laboratory experiments on granular flows suggest a linear profile of the horizontal velocity [e.g. *Azanza*, 1998; *Douady et al.*, 1999]. A weak influence of the vertical profile of the horizontal velocity has been observed by *Pouliquen and Forterre* [2002] for granular flows over inclined plane. We note that, in the locally tangent frame of reference, simple assumptions for the velocity profile (i.e. constant or linear profile) can be made unlike in the Galilean fixed reference frame. We assume here a vertically constant velocity so that $\overline{u_i u_j} = \bar{u}_i \bar{u}_j$. In the following, the overline will be dropped and (u, v) will represent the mean velocity field.

3 Flow and friction law

3.1 Simple friction law

A relation deduced from the mechanical behavior of the material has to be imposed between $\overline{\sigma}_{ij}$, T_{ti}, $\mathbf{u}$ and h in order to close equations (2.6)-(2.7) and (2.8). We consider here the minimal model, by using the hydrostatic assumption, i.e. $\overline{\sigma}_{ij} = 0$, $i \neq j$ and $\sigma_{xx} = \sigma_{yy} = \sigma_{zz}$. The depth-averaged mass is then considered as an effective material submitted to empirical frictions, introduced in the traction term T_{ti} in a way similar to the experimental approach by *Pouliquen* [1999].

Dissipation in granular materials is generally described by means of a Coulomb-type friction law, relating the tangential traction T_t on the bed to the normal stress $T_n = \sigma_{zz}|_b$ through a factor $\mu = \tan\delta$ involving the dynamic bed friction angle δ, namely

$$||T_t|| \leq \sigma_c = \mu ||T_n||,$$

which is acting opposite to the velocity. The value of σ_c defines the upper bound of the admissible stresses. In the coordinate system considered above, using the equation (2.9), we have

$$\sigma_c = \mu \rho g \gamma_z h.$$

The resulting Coulomb-type behavior can be summarized as follows,

$$\|T_t\| \geq \sigma_c \quad \Rightarrow \quad T_{ti} = -\sigma_c \frac{u_i}{\|\mathbf{u}\|}, \tag{3.1}$$

$$\|T_t\| < \sigma_c \quad \Rightarrow \quad \mathbf{u} = 0, \tag{3.2}$$

with $i = x, y$.

3.2 Flow variable friction law

Laboratory experiments [see *Pouliquen*, 1999] have shown that laws involving constant friction angle are restricted to granular flows over smooth inclined planes or flows over rough bed with high inclination angles. The assumption of constant friction angle seems to fail for granular flows over rough bedrock in a range of inclination angles for which steady uniform flows can be observed [*Pouliquen*, 1999]. In this range, the frictional force is able to balance the gravity force, indicating a shear rate dependence.
Pouliquen [1999] proposed to choice an empirical friction coefficient μ as function of the Froude number $\|u\|/\sqrt{gh}$ and the thickness h of the granular layer, in the form

$$\mu(\|u\|, h) = \tan\delta_1 + (\tan\delta_2 - \tan\delta_1) \exp\left(-\beta \frac{h}{d} \frac{\sqrt{gh}}{\|u\|}\right), \tag{3.3}$$

where δ_1, δ_2 and d are characteristics of the material which can be measured from the deposit properties. In particular, d is a characteristic length of the friction law, which is scaled on the mean diameter of particles; in the case of spherical glass particles used in these laboratory experiments d is of the order of the diameter of the beads and $\beta = 0.136$ [*Pouliquen*, 1999]. Equation (3.3) provides a friction angle, ranging between two values δ_1 and δ_2, depending on the values of the velocity and the flow thickness. The friction is higher for small values of the thickness and high values of the velocity, contrary to the function proposed by *Gray et al.* [1999] where lowest elevations (i.e. the rear and the front) are subject to small friction. What this empirical law means in terms of microscopic forces is still an open problem. Hydraulic models using this flow law has been shown to be able to predict the spreading of a granular mass from released to deposit [*Pouliquen and Forterre*, 2002].

Finally, if $\|T_t\| \geq \sigma_c$, the granular mass is flowing following the dynamical equations

$$\frac{\partial}{\partial t}(h\bar{u}) + \frac{\partial}{\partial x}(h\bar{u}^2) + \frac{\partial}{\partial y}(h\bar{u}\bar{v}) = \gamma_x g h + \frac{\partial}{\partial x}(g\gamma_z \frac{h^2}{2}) - \mu g \gamma_z h \frac{u_x}{\|\mathbf{u}\|}, \tag{3.4}$$

$$\frac{\partial}{\partial t}(h\bar{v}) + \frac{\partial}{\partial x}(h\bar{u}\bar{v}) + \frac{\partial}{\partial y}(h\bar{v}^2) = \gamma_y g h + \frac{\partial}{\partial y}\left(g\gamma_z \frac{h^2}{2}\right) - \mu g \gamma_z h \frac{u_y}{\|\mathbf{u}\|}, \tag{3.5}$$

and, if $\|T_t\| < \sigma_c$, the granular mass stops, i.e. $\mathbf{u} = 0$.

4 Numerical Model

4.1 Finite volume method

The model developed here is based on the classical finite volume approach for solving hyperbolic systems, using the concept of cell-centered conservative quantities. This type of methods requires the formulation of the equations in terms of conservation laws. The system of equations (2.6) and (3.4)-(3.5) can be rewritten as

$$\frac{\partial \mathbf{U}}{\partial t} + \operatorname{div} \mathbf{F}(\mathbf{U}) = \mathbf{B}(\mathbf{U}), \tag{4.1}$$

with

$$\mathbf{U} = \begin{pmatrix} h \\ q_x \\ q_y \end{pmatrix}, \quad \mathbf{F}(\mathbf{U}) = \begin{pmatrix} q_x & q_y \\ \frac{q_x^2}{h} + \frac{g}{2}h^2 & \frac{q_x q_y}{h} \\ \frac{q_x q_y}{h} & \frac{q_y^2}{h} + \frac{g}{2}h^2 \end{pmatrix}, \tag{4.2}$$

$$\mathbf{B}(\mathbf{U}) = \begin{pmatrix} 0 \\ gh\gamma_x - \sigma_{xz}|_b \\ gh\gamma_y - \sigma_{yz}|_b \end{pmatrix}, \tag{4.3}$$

where $\mathbf{q} = h\mathbf{u}$ is the material flux.

The equations are discretized on general triangular grids with a finite element data structure, using a particular control volume which is the median based dual cell (Figure 4.1a). The finite element grid is appropriate to describe variable topography and refinement is performed when strong topographic gradients occur. Dual cells C_i are obtained by joining the centers of mass of the triangles surrounding each vertex P_i. We also use the following notations:

- K_i, set of nodes P_j surrounding P_i,
- $|C_i|$, area of C_i,
- Γ_{ij}, boundary edge belonging to cells C_i and C_j,
- L_{ij}, length of Γ_{ij},
- $\mathbf{n}_{ij}$, unit normal to Γ_{ij}, outward to C_i.

If P_i is a node belonging to the boundary Γ of the numerical domain, we join the centers of mass of the triangles adjacent to the boundary to the middle of the edge belonging to Γ (see Figure 4.1b).

Let Δt denote the time-step, $\mathbf{U}_i^n$ is the approximation of the cell-average of the exact solution at time $t^n = n\Delta t$, $n \in \mathbb{N}$, i.e.

$$\mathbf{U}_i^n \simeq \frac{1}{|C_i|} \int_{C_i} \mathbf{U}(t^n, x) dx,$$

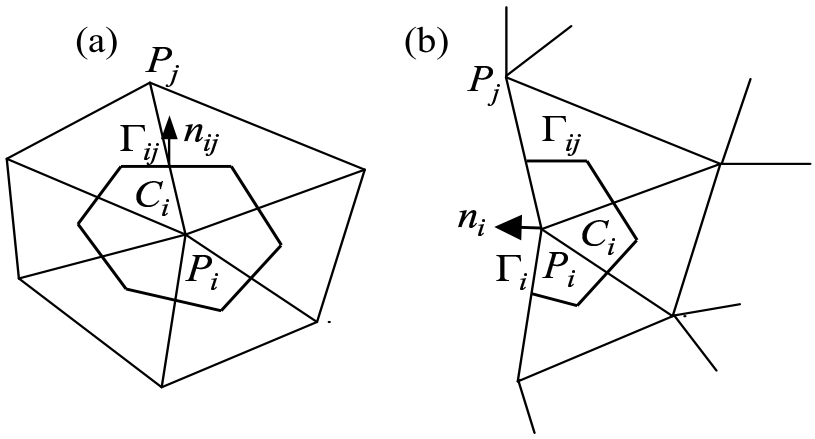

Figure 4.1: Triangular finite element mesh: (a) dual inner cell C_i, (b) dual boundary cell C_i.

and $\mathcal{B}(\mathbf{U}_i^n)$ is the approximation of the cell-average of the exact source term,

$$\mathcal{B}(\mathbf{U}_i^n) \simeq \frac{1}{|C_i|} \int_{C_i} \mathbf{B}(\mathbf{U}(t^n, x))dx.$$

Then, the finite volume scheme reads

$$\mathbf{U}_i^{n+1} = \mathbf{U}_i^n - \sum_{j \in K_i} \alpha_{ij} \; \mathcal{F}\left(\mathbf{U}_i^n, \mathbf{U}_j^n, \mathbf{n}_{ij}\right) - \Delta t \mathcal{B}\left(\mathbf{U}_i^n\right), \tag{4.4}$$

with

$$\alpha_{ij} = \frac{\Delta t L_{ij}}{|C_{ij}|}, \tag{4.5}$$

and $\mathcal{F}\left(\mathbf{U}_i^n, \mathbf{U}_j^n, \mathbf{n}_{ij}\right)$ denotes an interpolation of normal components of the flux $\mathbf{F}(\mathbf{U}) \cdot \mathbf{n}_{ij}$ along the edge Γ_{ij}. The treatment of the boundary conditions, namely the calculation of the boundary fluxes, using a Riemann invariant is addressed in *Bristeau et al.* [2001].

The main difficulty is to compute numerical fluxes at the control volume interfaces Γ_{ij} and the overall stability of the method requires some upwinding in the interpolation of the fluxes [see *Audusse et al.*, 2000]. The computation of these fluxes constitutes the major difference between the kinetic scheme used here and Godunov-type methods, which are usually very accurate for shock-capturing but not well suited to deal with vacuum front at the margins of the avalanche where the system looses hyperbolicity ($h = 0$ corresponding to dry soils). This drawback results from the lack of definable wave speeds in advance of a flow front. Many shock-capturing upwind schemes produce negative heights of water at these points and subsequently they break down or become unstable. An artificial small height of

fluid in the whole domain has to be imposed to stabilize the scheme [e.g. *Mangeney et al.*, 2000]. *Tai* [2000] and *Tai et al.* [2002] overcome this imperfection by tracking the vacuum front. *Denlinger and Iverson* [2001] calculate the theoretical speed of a flow front using the Riemann invariant of the wave emanating from the front directed in the inner part of the mass.

We follow here an alternative approach to solve Saint-Venant equations by using a kinetic solver, which is intrinsically able to treat vacuum and is appropriate to handle discontinuous solutions. These properties are of the highest importance for gravitational flow modelling. One further important property of this scheme is that it does not require any dimensional splitting. Kinetic schemes might be one of the best compromise between accuracy, stability and efficiency for the resolution of Saint-Venant equations [see *Audusse et al.*, 2000]. To our knowledge, this type of schemes has never been applied to avalanche flow modelling over slopping topography.

4.2 Kinetic formulation

The kinetic approach consists in using a fictitious description of the microscopic behavior of the system, in order to define numerical fluxes at the interface of an unstructured mesh. In fact, the macroscopic discontinuities disappear at the microscopic scale. We introduce here the main concepts of the kinetic scheme used for this model; a more complete description and deatils about its numerical implementation are done in *Audusse et al.* [2000] and *Bristeau et al.* [2001]. The scheme will be discussed by omitting the friction term, which is further introduced by using a semi-implicit scheme (see Section 4.3). In this method, fictitious particles are introduced and the equations are considered at the microscopic scale, where no discontinuities occur. A distribution function $M(t,x,y,\xi)$ of fictitious particles with microscopic velocity ξ is introduced to obtain a linear microscopic kinetic equation equivalent to macroscopic equation (4.1), with (4.2)-(4.3). The microscopic density of particles present at time t in the vicinity $\Delta x\,\Delta y$ of the position (x,y) and with velocity ξ is given by

$$M(t,x,y,\xi) = \frac{h(t,x,y)}{c^2}\,\chi\left(\frac{\xi - \mathbf{u}(t,x,y)}{c}\right), \tag{4.6}$$

with "fluid density" h, "fluid temperature" proportional to

$$c^2 = \frac{gh}{2}, \tag{4.7}$$

and $\chi(\omega)$ a positive even function defined on $\Re^2$ and satisfying

$$\int_{\Re^2} \chi(\omega)d\omega = 1, \quad \int_{\Re^2} \omega_i\omega_j\chi(\omega)d\omega = \delta_{ij}, \tag{4.8}$$

with δ_{ij} the Kronecker symbol and $\omega = (\omega_i, \omega_j)$. This function χ is assumed to be compactly supported, i.e.

$$\exists\, \omega_M \in \Re \;\text{ such that }\; \chi(\omega) = 0, \quad \text{for } |\omega| \geq \omega_M. \tag{4.9}$$

Note that the rectangular shape of the distribution function χ imposed for the fictitious particles would change in time if real particles where considered.

Simple calculations show that the macroscopic quantities are linked to the microscopic density function by the following relations,

$$\mathbf{U} = \int_{\Re^2} \begin{pmatrix} 1 \\ \xi \end{pmatrix} M(t,x,y,\xi) d\xi, \tag{4.10}$$

$$\mathbf{F}(\mathbf{U}) = \int_{\Re^2} \begin{pmatrix} \xi \\ \xi \otimes \xi \end{pmatrix} M(t,x,y,\xi) d\xi, \tag{4.11}$$

$$\mathbf{B}_i(\mathbf{U}) = g\gamma_i \int_{\Re^2} \begin{pmatrix} 1 \\ \xi \end{pmatrix} \nabla_\xi M(t,x,y,\xi) d\xi, \tag{4.12}$$

with $i = x, y$. These relations imply that the nonlinear system (2.6) and (3.4)-(3.5) is equivalent to the linear transport equation for the quantity M, for which it is easier to find a simple numerical scheme with good properties,

$$\frac{\partial M}{\partial t} + \xi \cdot \nabla_{\mathbf{x}} M - g\,\boldsymbol{\gamma} \cdot \nabla_\xi M = Q(t,x,y,\xi), \tag{4.13}$$

for some collision term $Q(t,x,y,\xi)$ which satisfies

$$\int_{\Re^2} \begin{pmatrix} 1 \\ \xi \end{pmatrix} Q(t,x,y,\xi) d\xi = 0. \tag{4.14}$$

As usual, the collision term $Q(t,x,y,\xi)$ in this kinetic representation of the Saint-Venant equations, which relaxes the kinetic density to the microscopic equilibrium M, is neglected in the numerical scheme, i.e. at each time-step we project the kinetic density on M, which is a way to perform all the collisions at once and to recover the Gibbs equilibrium without computing it [see *Perthame and Simeoni*, 2001].

Finally, the discretization of this simple kinetic equation allows us to deduce an appropriate discretization of the macroscopic system. A simple upwind scheme is applied to the microscopic equation (4.13), leading to the formulation of the fluxes defined in equation (4.4),

$$\mathcal{F}(\mathbf{U}_i, \mathbf{U}_j, \mathbf{n}_{ij}) = \mathbf{F}^+(\mathbf{U}_i, \mathbf{n}_{ij}) + \mathbf{F}^-(\mathbf{U}_j, \mathbf{n}_{ij}), \tag{4.15}$$

$$\mathbf{F}^+(\mathbf{U}_i, \mathbf{n}_{ij}) = \int_{\xi\cdot\mathbf{n}_{ij}\geq 0} \xi \cdot \mathbf{n}_{ij} \begin{pmatrix} 1 \\ \xi \end{pmatrix} M_i(\xi) d\xi, \tag{4.16}$$

$$\mathbf{F}^-(\mathbf{U}_j, \mathbf{n}_{ij}) = \int_{\xi\cdot\mathbf{n}_{ij}\leq 0} \xi \cdot \mathbf{n}_{ij} \begin{pmatrix} 1 \\ \xi \end{pmatrix} M_j(\xi) d\xi. \tag{4.17}$$

The simple form of the density function (here a rectangle-type function Π) allows analytical resolution of integrals (4.16)-(4.17) and gives the possibility to write directly a finite volume formula, which therefore avoids using the extra variable ξ in the implementation of the code. The resulting numerical scheme is consistent and conservative. Furthermore, it is proved

that the water height positivity is preserved under the Courant-Friedrichs-Levy condition [see *Audusse et al.*, 2000],

$$\Delta t \max\left(|u_i^n| + \omega_M c_i^n\right) \leq \frac{|C_i|}{\sum_{j \in K_i} L_{ij}}. \tag{4.18}$$

In comparison with flood modelling, avalanche modelling introduces a further difficulty relating to the property of granular media to be able to remain static (solid) even with an inclined free surface. This equilibrium is not intrinsically preserved by finite volume schemes and specific processing has to be introduced in the numerical scheme for the particular case of kinetic scheme, as it will be developed in the next section.

4.3 Friction

The friction is introduced in two steps. A first estimation of the numerical fluxes $\tilde{\mathbf{q}}_i^{n+1}$ is obtained by solving equation (4.4) without any friction term and the flow thickness h_i^{n+1} is calculated by solving explicitly the mass conservation (2.6). As friction does not change the direction of the velocity, we impose that the corrected flux $\mathbf{q}_i^{n+1}$ has the same direction of $\tilde{\mathbf{q}}_i^{n+1}$.
If the norm of the driving force $\tilde{\mathbf{q}}_i^{n+1}/\Delta t$ is lower than the Coulomb threshold $\sigma_c/\rho = \mu g \gamma_z \; h_i^{n+1}$, then the mass stops, i.e.

$$||\tilde{\mathbf{q}}_i^{n+1}|| - \mu g \gamma_z \; h_i^{n+1} \Delta t \leq 0 \;\Rightarrow\; \mathbf{q}_i^{n+1} = 0. \tag{4.19}$$

On the other hand, if the driving force $\tilde{\mathbf{q}}_i^{n+1}/\Delta t$ is higher than the Coulomb threshold, then the norm of the friction term $\sigma|_b$ is equal to σ_c.
Following *Bristeau et al.* [2001], we introduce a semi-implicit treatment of the friction term. Equation (4.4), written in terms of the variable $\mathbf{q}$, reads

$$\mathbf{q}_i^{n+1} = \left(||\tilde{\mathbf{q}}_i^{n+1}|| - \mu g \gamma_z \; h_i^{n+1} \Delta t\right) \frac{\tilde{\mathbf{q}}_i^{n+1}}{||\tilde{\mathbf{q}}_i^{n+1}||}. \tag{4.20}$$

This threshold-type behavior is generally not taken into account in numerical models, due to the resulting discontinuity in the velocity field. Generally, the magnitude of active and Coulomb friction forces is compared only for parts of the flow where $\mathbf{u} \neq 0$ [e.g. *Mangeney et al.*, 2000; *Eglit*, 1983].

Due to the possible space variations of h, classical kinetic schemes do not allow the mass stopping even though its velocity is equal to zero. In fact, for the kinetic scheme based on a rectangle-type distribution function χ as in equation (4.6), perturbations propagate at velocity $\tilde{c} = \sqrt{gh}$ even though the fluid is at rest because the "temperature" is not equal to zero.
In our case, perturbations linked to the h-gradient of a nonflat free surface generate fluxes and the fluid never stops. On the opposite, the Coulomb criterium imposes that, under a given threshold, a perturbation (of the surface elevation, for example) do not propagates.

It can be represented by a fluid at "temperature" equal to zero, so that the local speed of propagation of the disturbance relative to the moving stream is equal to zero. It can be obtained by using a Dirac distribution for the function χ.

The idea of the present scheme is to introduce a "zero-temperature fluid" with a Dirac-type density of particles M when the fluid is under the Coulomb threshold and a "nonzero-temperature fluid" using a rectangular-type density of particles when the fluid is over the Coulomb threshold, so we have

$$\|\tilde{\mathbf{q}}_i^{n+1}\| - \mu g \gamma_z \; h^{n+1} \Delta t < 0 \quad \Rightarrow \quad M(t,x,y,\xi) = h(t,x,y)\delta\left(\xi - \mathbf{u}(t,x,y)\right), \tag{4.21}$$

$$\|\tilde{\mathbf{q}}_i^{n+1}\| - \mu g \gamma_z \; h^{n+1} \Delta t \geq 0 \quad \Rightarrow \quad M(t,x,y,\xi) = \frac{h(t,x,y)}{c^2}\chi\left(\frac{\xi - \mathbf{u}(t,x,y)}{c}\right), \tag{4.22}$$

where the rectangular function χ given by *Bristeau et al.* [2001] reads

$$\chi(\omega) = \frac{1}{12}\Pi_{|\omega_i| \leq \sqrt{3}}, \quad i = 1,2. \tag{4.23}$$

The expression of the flux related to the edge Γ_{ij} in the mass conservation equation using (4.16) then reads

$$\|\tilde{\mathbf{q}}_i^{n+1}\| - \mu g \gamma_z \; h^{n+1} \Delta t < 0 \quad \Rightarrow \quad \mathbf{F}_h^+(\mathbf{U}_i, \mathbf{n}_{ij}) = h_i u_{i,n} Y(u_{i,n}), \tag{4.24}$$

$$\|\tilde{\mathbf{q}}_i^{n+1}\| - \mu g \gamma_z \; h^{n+1} \Delta t \geq 0, \quad \Rightarrow \quad \mathbf{F}_h^+(\mathbf{U}_i, \mathbf{n}_{ij}) = \frac{1}{2}h_i u_{i,n} + \frac{\sqrt{3}}{4}h_i c_i + \frac{1}{4\sqrt{3}}h_i \frac{u_{i,n}^2}{c_i} \tag{4.25}$$

where Y is the Heaviside distribution and $u_{i,n}$ is the velocity in the normal direction of the edge Γ_{ij}. Similar expressions are obtained for $\mathbf{F}^-(\mathbf{U}_j, \mathbf{n}_{ij})$.
Note that the Dirac distribution does not allow us to recover the momentum equation. In fact, the flux calculated for the momentum equation using this function reads

$$\mathbf{F}_m^+(\mathbf{U}_i, \mathbf{n}_{ij}) = h_i u_{i,n}^2 Y(u_{i,n}), \tag{4.26}$$

without the pressure gradient due to the zero-temperature fluid. However, when the fluid is under the Coulomb threshold, the momentum equation is replaced by $\mathbf{q} = 0$, so that the Dirac-type function is only used for the calculation of the fluxes in the mass conservation equation.

The first step of the numerical scheme is to evaluate the grid points that are under the Coulomb threshold using $\tilde{\mathbf{q}}_i^{n+1}$. We look at the simple 1D case (Figure 4.2) where the points P_0, P_1 and P_2 are under the Coulomb threshold (full circles) and the points P_3 and P_4 are above this threshold (stars). In order to obtain the flux $F_{h,i} = F_h^+(P_{i-1}) + F_h^-(P_i)$ at the interface M_i allowing to satisfy conservation laws, the same distribution function has to be used in both side of the interface: a rectangular distribution is imposed if one of the two points P_i or P_{i-1} is above the Coulomb threshold and a Dirac distribution elsewhere. As a result, the flux through the interface M_3 is calculated using a rectangular function whereas the flux through the interface M_2 is calculated using the Dirac function. The propagation of

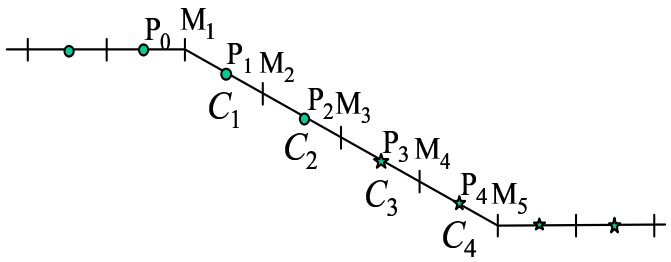

Figure 4.2: 1D mesh and dual cells C_i with center P_i (full circles denote the points under the Coulomb threshold and stars the points above the Coulomb threshold).

the h-gradient is then allowed to the right where the fluid is above the Coulomb threshold and forbidden to the left where the fluid is under the Coulomb threshold, recalling the typical solid-fluid transition of granular material. Numerical tests show that this method is mass conservative.

The resulting 2D scheme consists in evaluating at time t the points under the Coulomb threshold and in calculating at time $t + dt$ the flux F_h through the interface M_{ij} of a cell C_i

- using the rectangular distribution if one of the two points P_i and P_j situated on both sides of this interface is above the Coulomb threshold;
- using a Dirac distribution if the two points P_i and P_j are under the Coulomb threshold.

The numerical method is illustrated on the 2D mesh presented in Figure 4.3 where the points M_1, M_2, M_3, P_2, M_{10}, M_{11} surrounding the point P_1 are under the Coulomb threshold. The fluxes F_h through the interfaces of the cell C_1 is then calculated using the Dirac distribution, whereas in cell C_4 all the fluxes are calculated using the rectangular distribution. For the cell C_2, the surrounding points P_3 and M_8 being above the Coulomb threshold, the fluxes F_h through the edges cutting P_2M_8, P_2P_3 are calculated using the rectangular distribution, while the fluxes F_h through the edges cutting P_2P_1, P_2M_3, P_2M_9, P_2M_{10} are calculated using the Dirac distribution. With this scheme, verifying the mass conservation at the machine accuracy, the fluid is able to stop.

5 Validation

The precision and performance of the numerical model is tested by comparing numerical results with those of an analytical solution, which takes into account a Coulomb-type friction on the base of the flow, provided the angle of friction is smaller than the slope angle and the fluid never stops on the inclined plane [see *Mangeney et al.*, 2000].

The test case consists of the instantaneous release of a fluid mass of $1\,m$ high on a dry flat bottom, infinitely long in the negative x-direction. The numerical domain ranges from

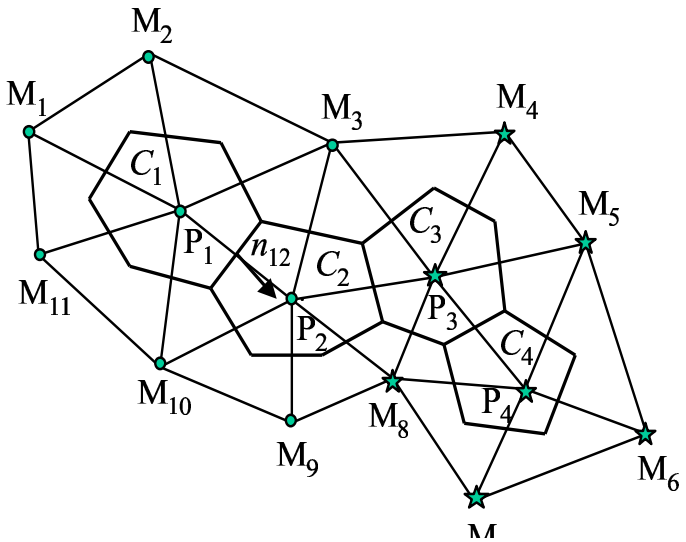

Figure 4.3: Triangular mesh and dual cell C_1, C_2, C_3 and C_4 (full circles denote the points under the Coulomb threshold and stars the points above the Coulomb threshold).

$0\,m$ to $2000\,m$. Note that the aspect ratio of the geometry considered here is $\epsilon = 10^{-3}$, so that the long waves approximation is valid. All 1D numerical experiments are carried out with the 2D model using the same number of points in the transversal direction (101 points with the same space-step as in the flow direction).
From Figure 5.1 and Figure 5.2, showing the comparison between analytical and numerical solution for two grid steps ($dx = 20\,m$ and $dx = 2\,m$), it can be observed that the numerical model provides a good representation of the dam-break problem as well without and with friction law. The main difference between analytical and numerical results is located at the front position and at the corner of the dam, as it was observed in *Mangeney et al.* [2000] with a Godunov-type numerical model. Note that the deviation from the analytical solution is qualitatively the same with the Godunov-type model and the kinetic model: the corner at the left discontinuity is rounded and the position of the front is lower than the position of the analytical front after a few seconds: the shock is smoothed, as usual with a first order scheme, as it was observed in *Audusse et al.* [2000]. Finally, the results are expressed in terms of the mean relative error

$$\mathrm{d}h = \frac{\Sigma\,(h - h_a)^2}{\Sigma h_a^2}, \tag{5.1}$$

where h_a is the analytical solution for h and Σ represents the sum over a fixed interval including the points where $0 < h < h_0$. Figure 5.3 shows that, when the space-step is reduced by a factor 10, the mean relative error is reduced by a factor about 4, which is

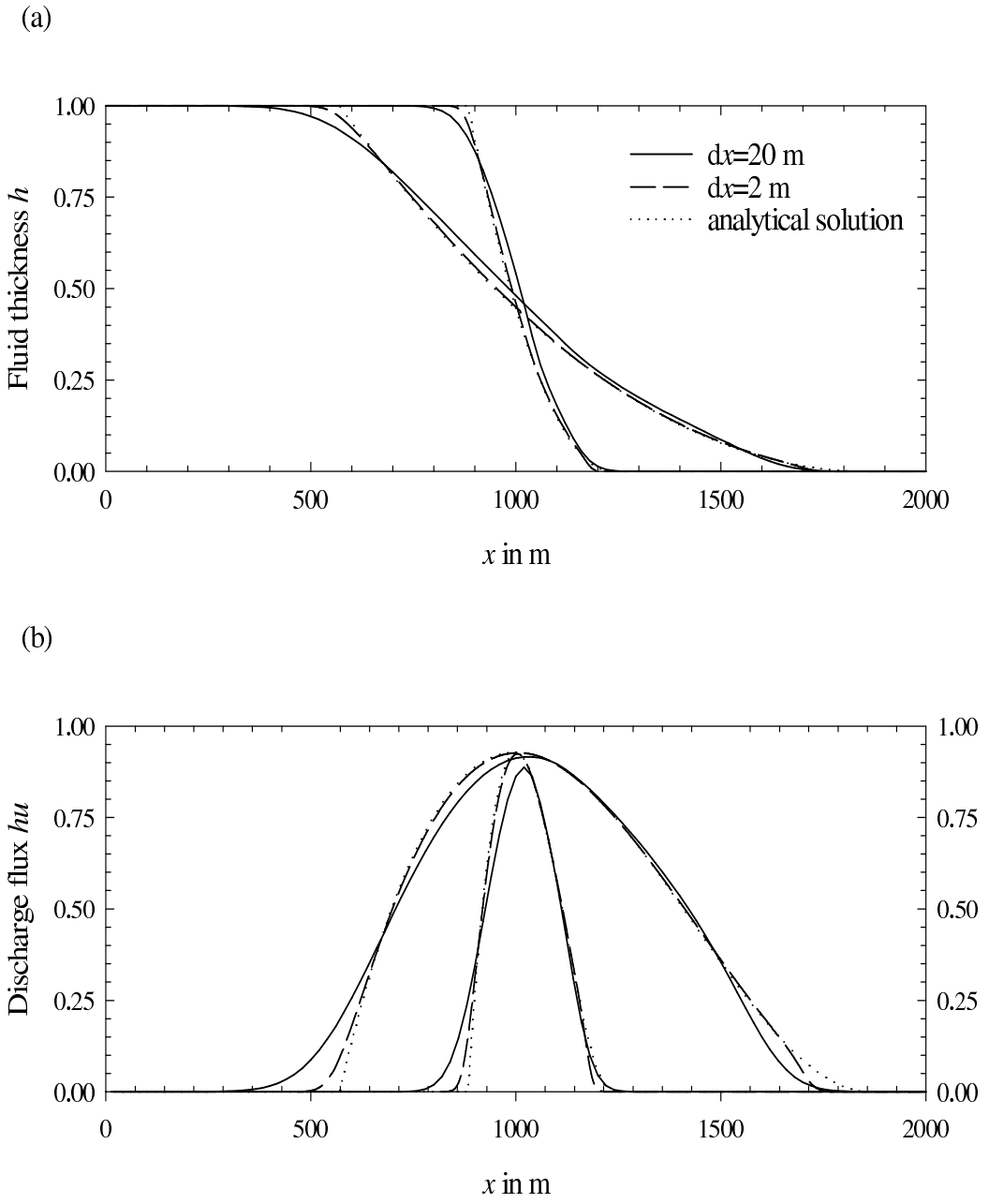

Figure 5.1: (a) Fluid thickness h and (b) discharge flux hu versus distance, obtained for $\delta = 0°$ and $\theta = 0°$ at time $t = 37\,s$ and $t = 137\,s$, calculated with the analytical solution (dotted lines) and with the numerical model for $dx = 20\,m$ (solid lines) and $dx = 2\,m$ (dashed lines).

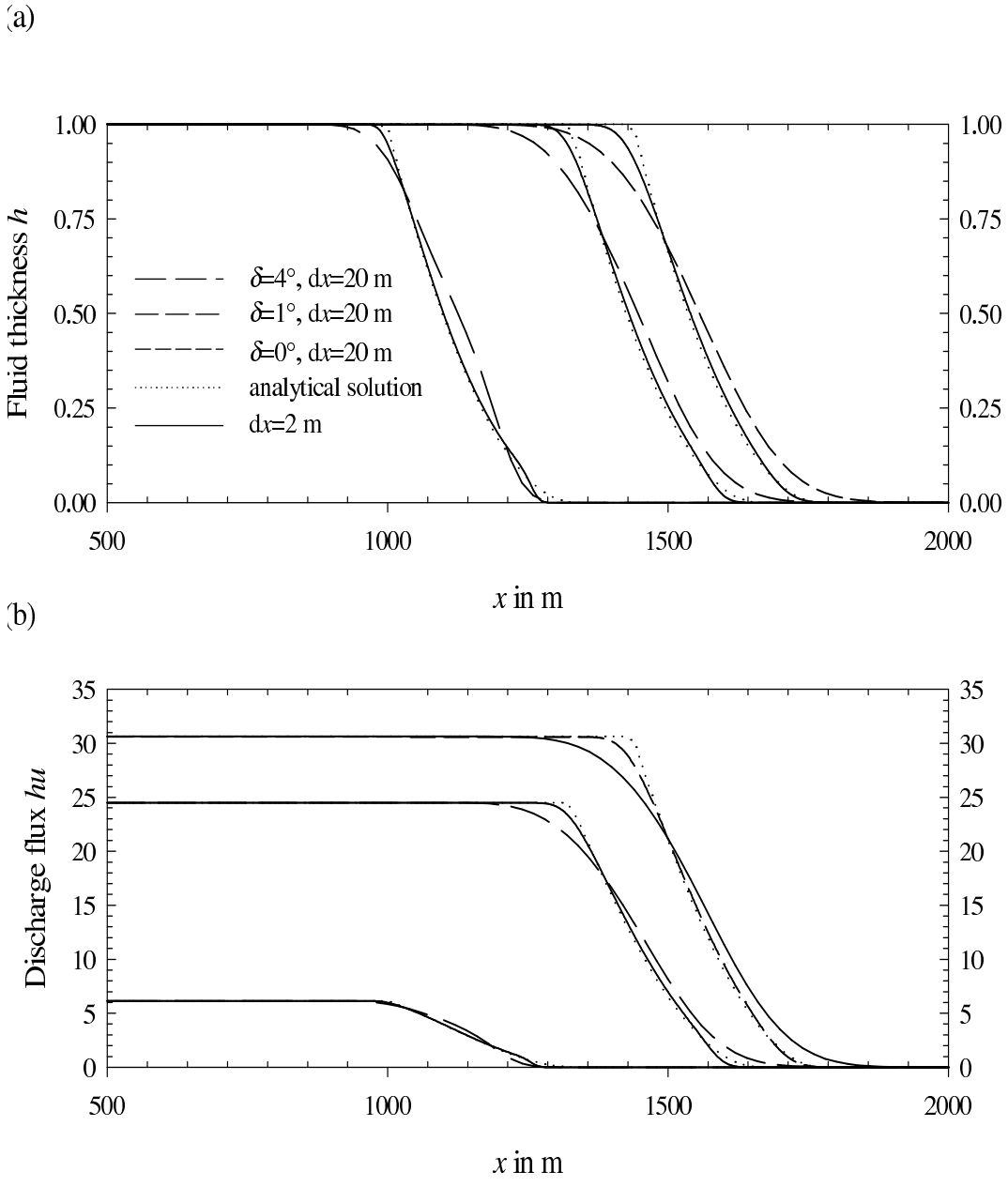

Figure 5.2: (a) Fluid thickness h and (b) discharge flux hu versus distance, obtained for $\delta = 0°$, $\delta = 1°$ and $\delta = 4°$ for inclination angle $\theta = 5°$ at time $t = 35\,s$, calculated with the analytical solution (dotted lines) and with the numerical model for $dx = 20\,m$ and $dx = 2\,m$ (solid lines).

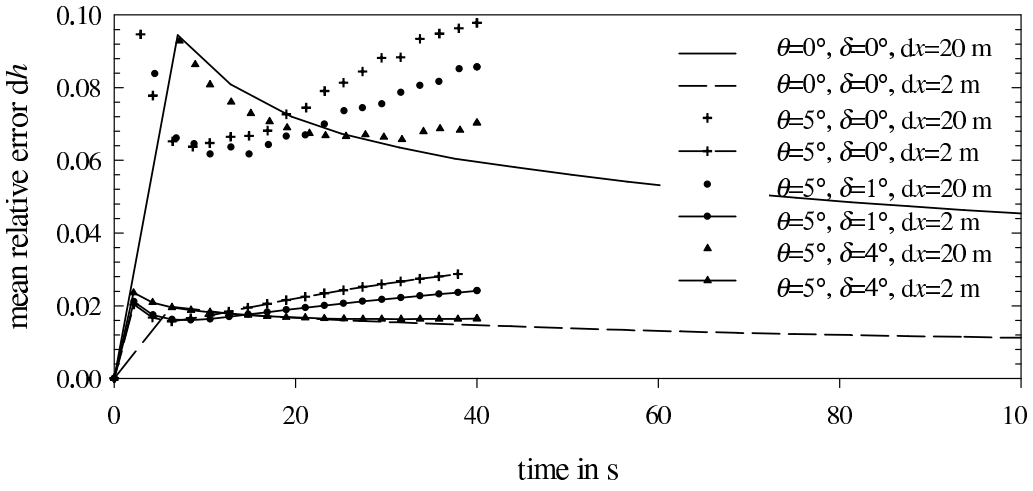

Figure 5.3: Mean relative error Δh for the dam-break problem for $dx = 20\,m$ (symbols) and and $dx = 2\,m$ (solid lines with symbols) for inclination angle of the bottom $\theta = 5°$ with various angle of friction $\delta = 0°$, $\delta = 1°$ and $\delta = 4°$ and mean relative error Δh for $\theta = 0°$ ($dx = 20\,m$ solid lines and $dx = 2\,m$ dashed lines).

compatible with other general convergence rates that can be proved for simple models in presence of singularities (e.g. *Perthame* [2002]). Similar results are obtained when the error on hu is considered.

6 One-dimensional simulation over simplified topography

To illustrate the potentiality of the numerical model, we have performed a series of numerical experiments using the friction laws described above over simplified 1D geometry. As an example, let us consider an exponential shape for the topography $Z(x)$, with characteristic dimensions of the order of the real topography of White River Valley in Montserrat island (Lesser Antilles) where an extensively studied debris avalanche occurred 26 December 1997 [*Sparks et al.*, 2002]. This debris avalanche with an estimated volume of about $40 - 45 \times 10^6\,m^3$ was caused by the failure of the upper south flank of the Soufriere Hills Volcano. Geological and numerical studies of this event have been performed and estimation of the thickness, velocity and runout distance of this debris avalanche are now available. The maximum deposit thicknesses range from $60\,m$ to $100\,m$. Front heights of about $20\,m$ are observed at a distance of $200\,m$ from the shoreline. It can be inferred from the observations

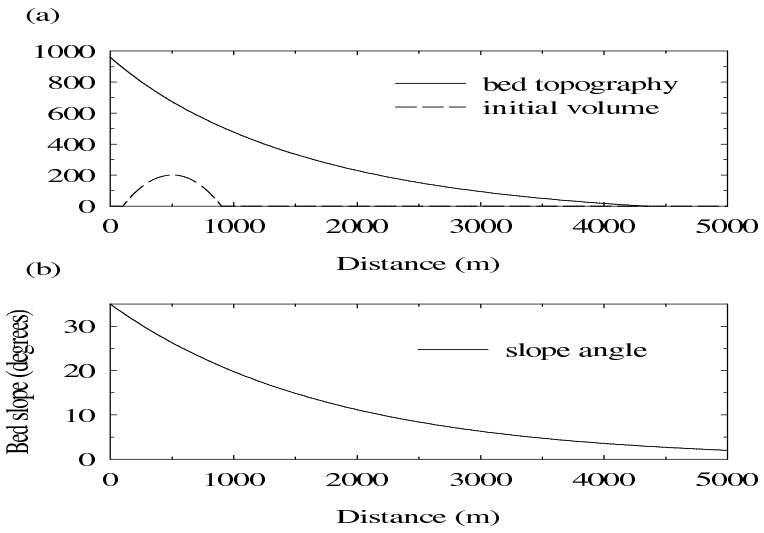

Figure 6.1: (a) Bed topography in Cartesian coordinates $(\tilde{x}, \tilde{z})$ and initial volume of the granular mass in topography-linked coordinates (x, z); (b) slope angle $\theta(x)$ of the bed in degrees in the topography-linked coordinates (x, z).

that the avalanche travels approximately $3.5\,km$ from the center of the destabilized mass, in the reference frame linked to the topography.

Let us investigate the influence of the various flow laws in the range of parameters allowing the mass to stop around the position $x = 4500\,m$, corresponding approximately to the observed runout of the Boxing Day debris avalanche down the White River Valley. In the White River Valley, the altitude decreases from $900\,m$ at the top of the avalanche with a maximum slope inclination of $35°$ to the sea, with slope inclination of a few degrees at the shore. The corresponding angle is defined by

$$\theta(x) = \theta_0 \exp\left(-\frac{x}{a}\right), \tag{6.1}$$

with $\theta_0 = 35°$ and $a = 1750\,m$ (Figure 6.1b). The summit is located at an altitude of $950\,m$ with an initial slope of $35°$, the topography being almost horizontal in the right part (Figure 6.1a). The results are presented in the coordinate system (x,z) linked to the topography. The initial conditions are defined by the instantaneous release of a parabolic mass over a rigid topography, represented in Figure 6.1a in the coordinate system (x,z) where

$$h(x, t = 0) = K\left(l - (x - x_0)^2\right), \tag{6.2}$$

$$u(x, t = 0) = 0, \tag{6.3}$$

with $K = 1.26 \times 10^{-3}\, m^{-1}$, $l = 1.6 \times 10^5\, m^2$ and $x_0 = 500\, m$. Initially, the maximal thickness of the mass is $200\, m$ in the direction perpendicular to the topography with a length of $800\, m$, close to the estimations of the Boxing Day debris avalanche destabilized mass. The numerical domain is discretized using 880 points in the x-direction with a space-step of $6.25\, m$.

6.1 Curvature effects

We note that equations (3.4)-(3.5) are obtained by neglecting the first order curvature terms. At first order in 1D, curvature effects lead to an additional friction force linked to centrifugal acceleration. According to the scale analysis of *Savage and Hutter* [1989], this first order curvature effect is taken into account by a term involving the curvature radius R of the bed profile in the momentum equation

$$\frac{\partial}{\partial t}(h\bar{u}) + \frac{\partial}{\partial x}(h\bar{u}^2) + \frac{\partial}{\partial y}(h\bar{u}\bar{v}) = \gamma_x g h + \frac{\partial}{\partial x}(g\gamma_z \frac{h^2}{2}) - \mu h (g\gamma_z + \frac{u^2}{R})\frac{u}{|u|}. \tag{6.4}$$

When either μ or $\lambda = L/R_c$, where R_c is a characteristic value of the curvature radius, or both are smaller than $O(\epsilon^{\frac{1}{2}})$ and when u does not become too large, then this term may be dropped in comparison with the others terms [see *Greve and Hutter*, 1993].

Numerical tests confirm that the first order curvature effects involved in the last term of equation (6.4) is not too large in our case, where the radius of curvature is relatively high. Note that, in the present case, ϵ is of order 0.1, $\mu = 0.27$ for $\delta = 15°$ is of order $\epsilon^{\frac{1}{2}}$ and λ is lower than 4×10^{-3}.

Figure 6.2 shows that the results with and without this curvature term are close to each other for a simple friction law with $\delta = 15°$, especially during the flow. Furthermore, the fluid stops almost at the same time ($t = 86.4\, s$ without curvature effects and $t = 86\, s$ with curvature effects) and the maximum elevation of the deposit is the same ($h_{max} = 67.8\, m$ without curvature and $h_{max} = 68\, m$ with curvature). However, a difference of $156\, m$ (5% of the deposit length) is observed in the runout distance.

When curvature effects are not taken into account, i.e. when the exponential shape does not slow down the granular mass, the front is located further away. The empirical nature of the friction angle in such a model is well illustrated in this example. In fact, curvature effects are difficult to take into account in 2D experiments. Dropping these effects leads to unverifiable error in the determination of the well-fitted friction angle. In the following 1D simulations, first order curvature effects have been also taken into account.

6.2 The Coulomb friction law

We first look at the results obtained by using the friction law with constant angle. Sensitivity study is performed just by varying the value of this angle. The avalanche deposit extends further for lower values of δ, as shown in Figure 6.3, where the geometry of the deposits is obtained when the flow comes to rest. A difference of approximatively $740\, m$ on the front position is obtained when δ varies from 14° to 16°, while a difference of approximatively $1060\, m$ when δ varies from 16° to 20°. Furthermore, the length of the deposit is larger

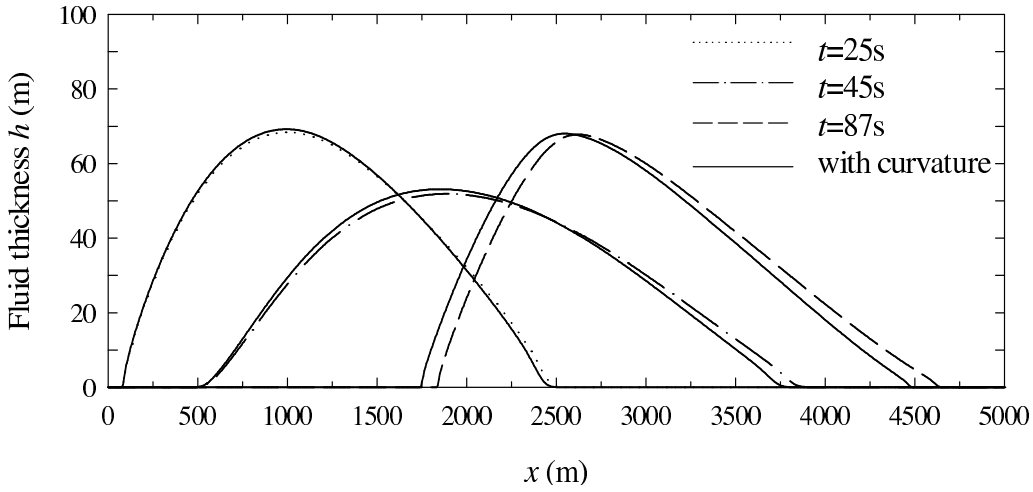

Figure 6.2: Fluid thickness h at $t = 25\,s$, $t = 45\,s$ and $t = 87\,s$ (i.e. when the fluid stops) with and without the curvature term for a simple friction law with $\delta = 15°$. The dash-dotted lines represent the result without curvature effect and the corresponding full lines those with curvature effect at the same time. Note that the fluid stops approximatively at the same time.

and the maximum elevation lower when the friction angle decreases. The deposit extends along $2900\,m$ when $\delta = 14°$ with a maximum elevation $h = 65\,m$, while the extension is only $2290\,m$ when $\delta = 20°$ with a maximum elevation $h = 75\,m$. It appears that only low values of the friction angle around 15° are appropriate to reproduce the great mobility of real debris avalanches, as it was observed in 2D simulation [see *Heinrich et al.*, 2001].

The low value of δ is a consequence of the widely observed ability of large avalanches to travel distances much larger than expected from classical models of slope failure. Note that, dispite of the extreme simplification of this test, the calculated values are in the range of the deposit elevation estimated from geological observation [see *Sparks et al.*, 2002]. The x-position of the maximum elevation is situated toward the rear of the mass. In fact, with a constant friction angle, in the accelerating stage, the fluid flows with higher velocity near the front than near the rear due to a driving negative h-gradient. The positive h-gradient near the downhill rear of the fluid plays a braking role in the balance of forces, as it is illustrated in Figure 6.4. It is worth pointing out that the force due to the pressure gradient (i.e. the h-gradient) is relatively small compared to the other forces as well, at $t = 25\,s$ as at $t = 65\,s$ in the rest of the mass. This feature may explain the weak effect of the parameter $k_{actpass}$ involved in the pressure gradient when non-isotropy of normal stresses is assumed [see *Pouliquen and Forterre*, 2002].

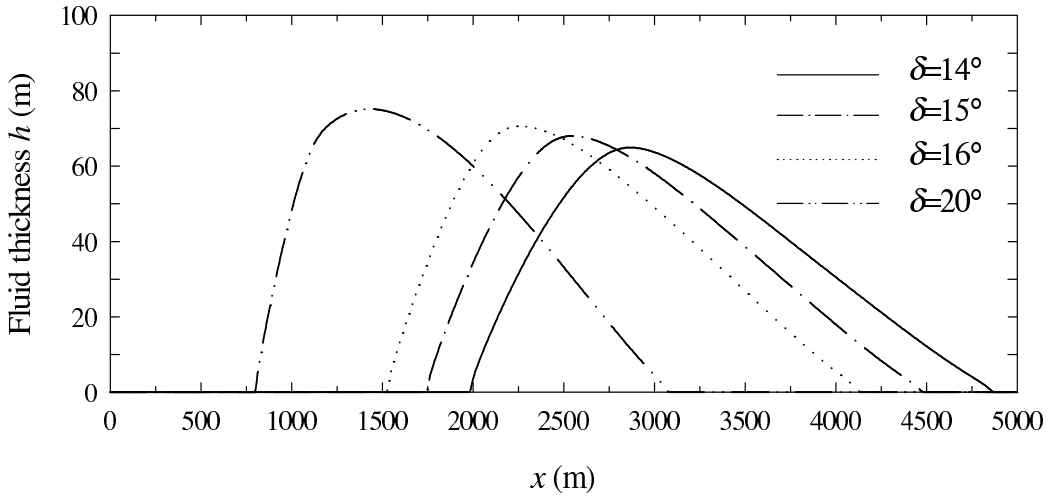

Figure 6.3: Profile of the mass at the time when the fluid stops, for various values of the friction angle δ using the simple friction law.

6.3 Pouliquen's friction law

We propose to use here the more recent law developed empirically by *Pouliquen* [1999] (see Section 3.2). Contrary to the one-parameter simple friction law, three parameters have to be determined: two friction angles δ_1, δ_2 and the coefficient d. Debris avalanches are composed of particles with sizes varying from less than one millimeter to tens of meters. It is therefore difficult to estimate the value of d in the model. However, a value of $d = 1.5\,m$ allows the mass reaching $x = 4500\,m$ for $\delta_1 = 13°$ and $\delta_2 = 20°$ (Figure 6.5). The variation of δ with the position is represented in Figure 6.6 at the instants $t = 25\,s$ and $t = 65\,s$ for $d = 1$, $d = 1.5$ and $d = 2$. Note that for low value of d the results are similar to those obtained for simple friction law with $\delta = 13°$ and for high values of d the results are close to those obtained using a simple friction law with $\delta = 20°$. In this range of values, the flow is governed by δ_2 near the front and the rear of the flow and by δ_1 in the inner part of the mass. The friction angle evolves in time as a function of the flow parameters $(h,\ hu)$ as in Figure 6.6. Differences of more than 1° are observed on δ when d-value goes from 1 to 2, leading to strong differences in the deposit (Figure 6.5). Figure 6.5 also shows that the shapes of the flowing mass at $t = 25\,s$ are similar for both various values of d and for the simple friction law. During the flowing stage, the friction force does not play a leading role, as it is illustrated in Figure 6.7a at $t = 25\,s$. During the deceleration stage, the importance of the friction forces increases (Figure 6.7b) to the stopping stage, where the friction forces balanced by the gravity force dominate the other forces. Concerning the deposit, not only the runout distance changes with d but also the shape. As d increases, the front becomes more marked and the rear finer. Such a shape seems to be closer to real

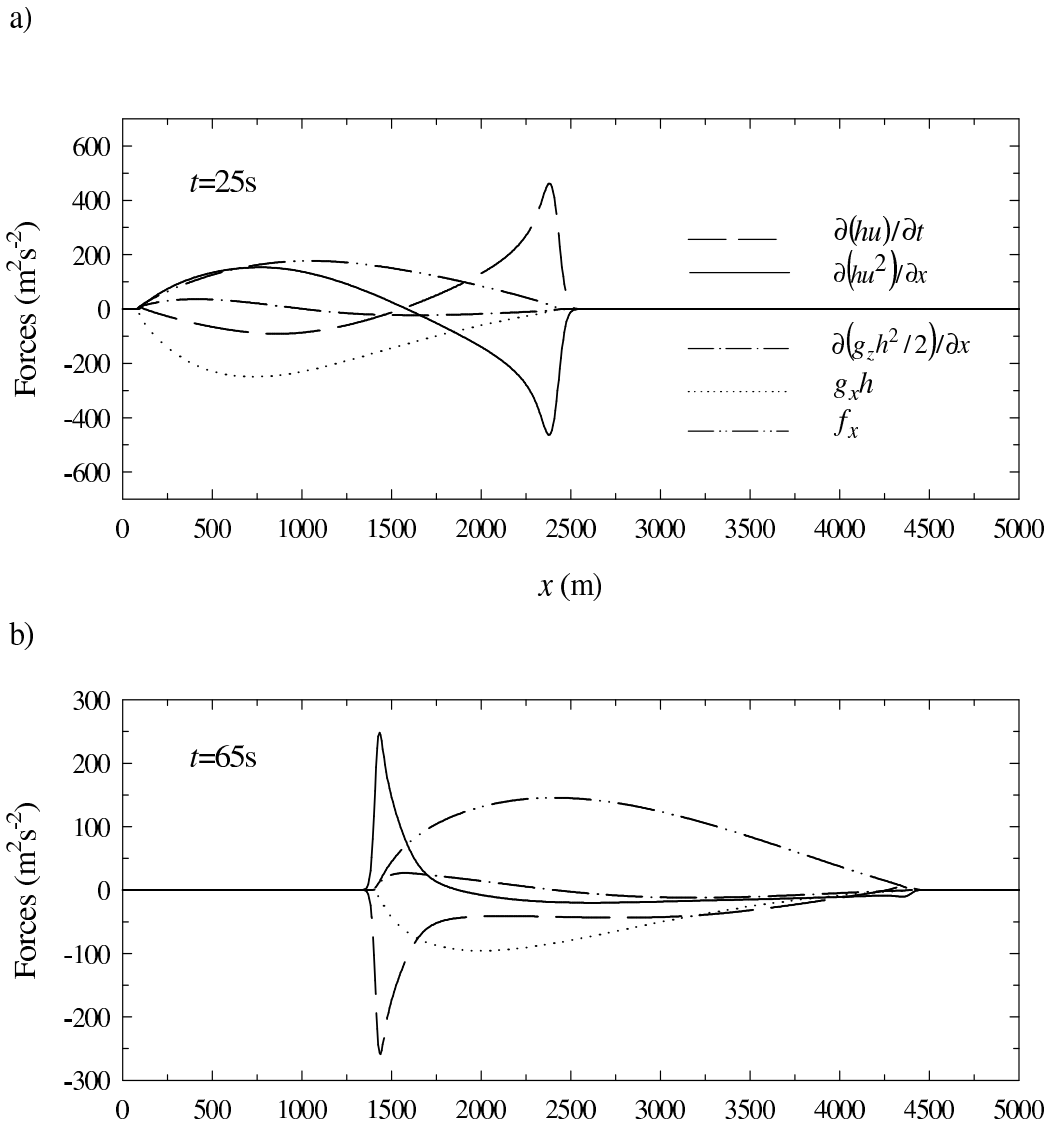

Figure 6.4: Forces involved in the x-momentum equation for a simple friction law with $\delta = 15°$ versus distance (a) at time $t = 25\,s$ and (b) at $t = 65\,s$.

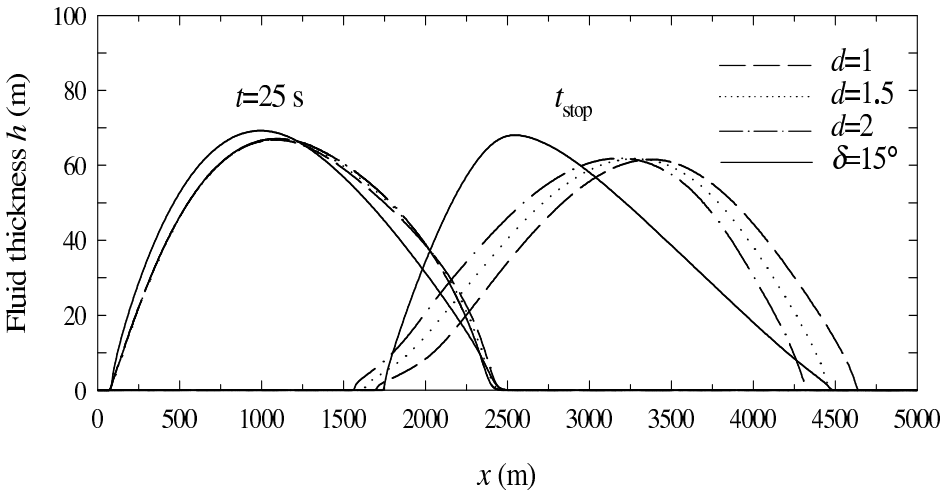

Figure 6.5: Fluid thickness at $t = 25\,s$ and when the fluid stops for various values of d in the Pouliquen's flow law, with $\delta_1 = 13°$ and $\delta_2 = 20°$, and for a simple friction law with $\delta = 15°$. The dash-dotted lines represent the result for the Pouliquen's flow law and the corresponding full lines those for the simple friction law.

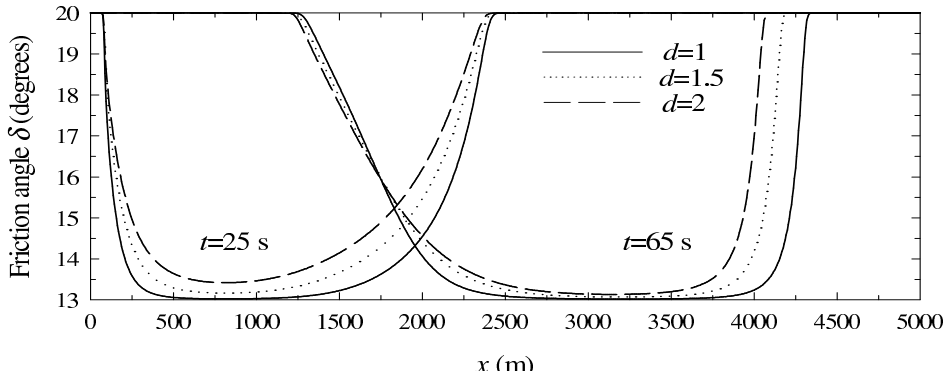

Figure 6.6: Friction angle δ versus position x in Pouliquen's flow law with $\delta_1 = 13°$ and $\delta_2 = 20°$ and $d = 1$ (full lines), $d = 1.5$ (dotted lines) and $d = 2$ (dashed lines) at time $t = 25\,s$ and $t = 65\,s$. At the rear and the front, i.e. for small values of h, the friction angle tends to δ_2.

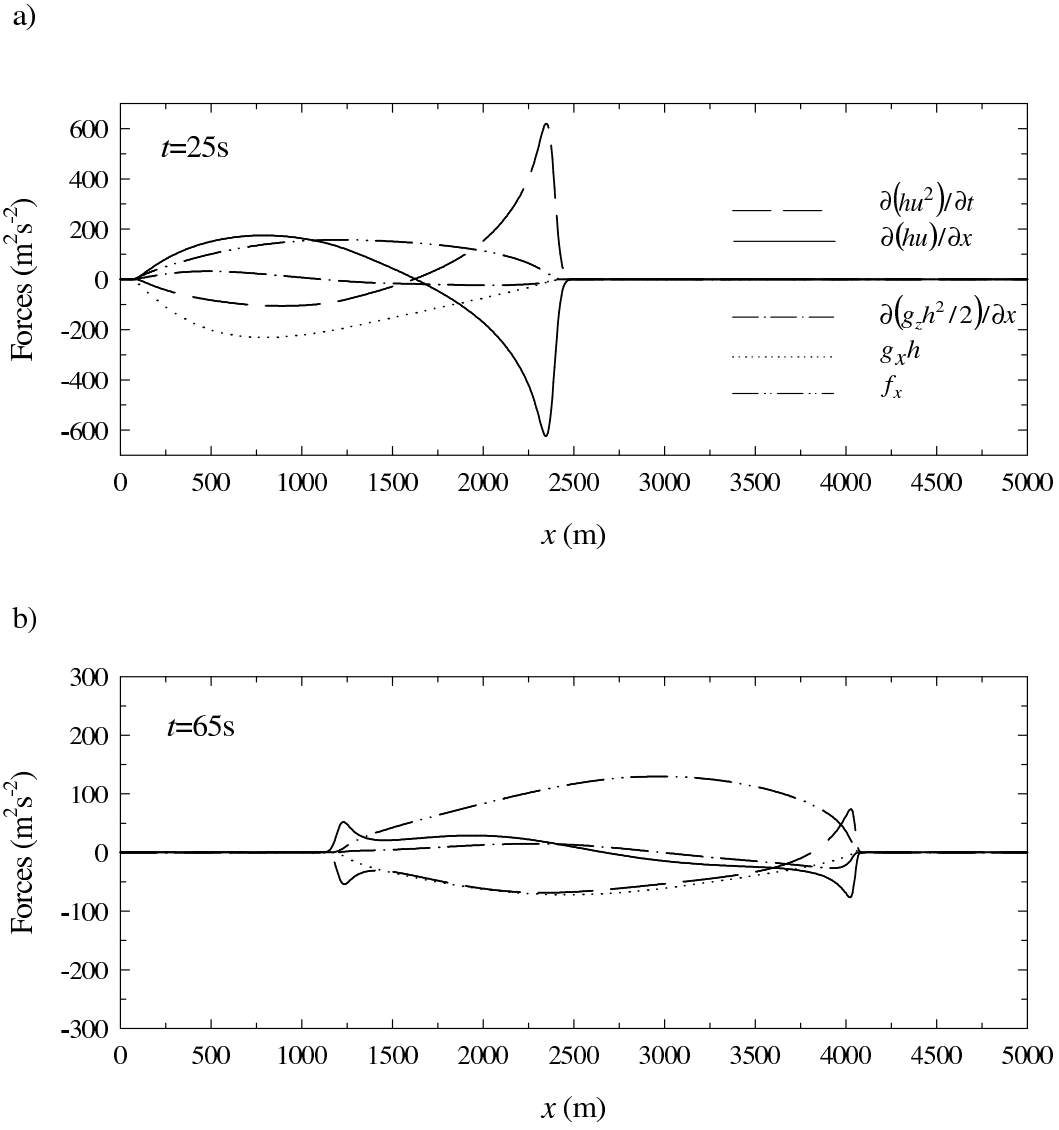

Figure 6.7: Forces involved in the x-momentum equation for Pouliquen's flow law with $\delta_1 = 13°$, $\delta_2 = 20°$ and $d = 1.5$ versus distance at time (a) $t = 25\,s$ and (b) $t = 65\,s$.

observed front of avalanches. The shape of the deposit using Pouliquen's friction law with $d = 1.5$ is quite different from that obtained by simple friction law with $\delta = 15^\circ$ even though the runout distance is the same and the extension of the deposit is similar (see Figure 6.5). The downhill part of the deposit using this variable friction angle is $18\,m$ high at $250\,m$ from the rear and $35\,m$ high for constant friction angle. Contrary to simple friction law, the maximum thickness is situated near the front for Pouliquen's flow law, due to low friction for high elevation in the inner part of the avalanche. In this example, contrary to simple friction law, Pouliquen's flow law can describe front height of approximatively $20\,m$ at a distance of $200\,m$ from the runout distance. As it was observed for simple friction law, the force due to the pressure gradient is relatively small compared with the other forces as well at $t = 25\,s$ as at $t = 65\,s$, except at the front (Figure 6.7).

These simple 1D simulations are in agreement with the results obtained using 2D simulations by *Heinrich et al.* [2001], where comparisons between flows calculated by Coulomb and Pouliquen's friction laws have shown the importance of the dependence of the friction angle on the Froude number and the flow height, suggesting a rate dependence in the mechanical behavior of debris avalanches.

6.4 Mass stopping

The major originality of the model presented in this paper consists in the introduction of the stopping mechanism in kinetic schemes. Let us look with more details at this stopping stage, illustrated in Figure 6.8 and Figure 6.9 for simple friction law and Pouliquen's flow law respectively.

For the simple friction law ($\delta = 15^\circ$) the mass stops at $t = 86\,s$ and for the Pouliquen's flow law ($\delta_1 = 13^\circ$, $\delta_2 = 20^\circ$ and $d = 1.5$) at $t = 97.6\,s$. With these rheological parameters, the runout distance for both simple friction law and Pouliquen's flow law is approximatively $4500\,m$. With the constant angle friction law, the front encountering low slope begins to stop. The stopping propagates toward the rear of the mass until the whole fluid stops. The asymmetric shape becomes more pronounced when the fluid stops, due to this downward propagation of the stopping stage. Note that, with this topography and with this initial released mass, the Coulomb threshold is never reached in the rear of the flow for friction angle higher than $\delta = 23^\circ$. For such high friction, the front stops and this stopping propagates toward the rear. However, the driving force and in particular the gravity near the rear of the flow is still higher than the Coulomb threshold due to high slope of the topography. In this case, the h-gradient may play a significant role in controlling the balance of forces. As an example, at $t = 70\,s$ for $\delta = 24^\circ$, the whole fluid is stopping except a $150\,m$ long part in the rear of the mass. In this region, the fluid is stopped by the downhill mass which is under the Coulomb threshold. The presence of a fluidized zone behind a rigid mass would be an interesting point to verify by comparing numerical results derived from mathematical models with empirical or geological observation of deposits. The stopping scenario is not the same for Pouliquen's flow law, for which the central part of the fluid is stopping first. In this case, the friction angle is not constant, as it was observed in the previous section.

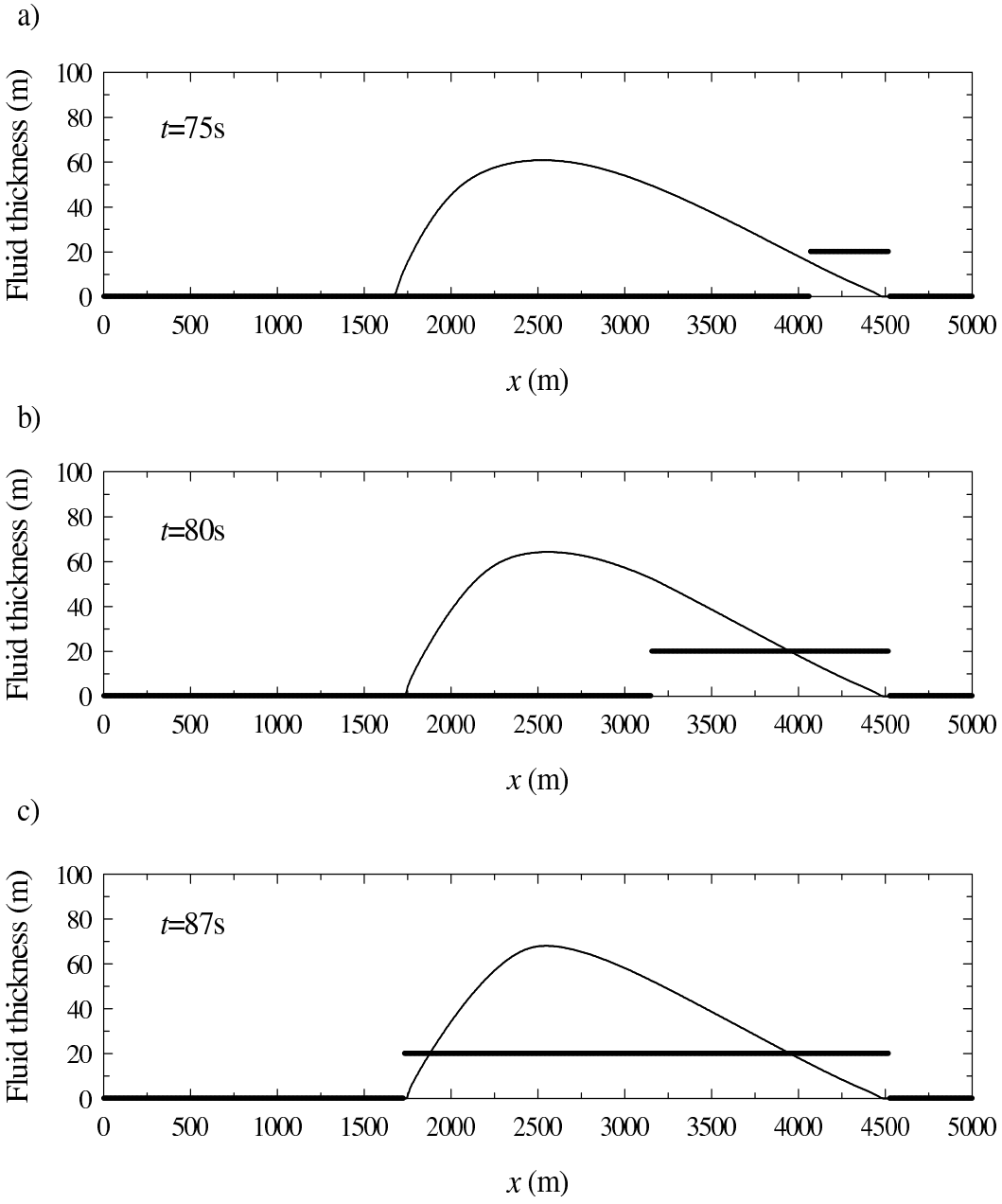

Figure 6.8: Fluid thickness (full lines) versus distance at (a) $t = 75\,s$, (b) $t = 80\,s$ and (c) $t = 87\,s$ during the stopping stage for simple friction law with $\delta = 15°$. A value of 0 is allocated to the fluid under the Coulomb threshold and a value of 20 to the fluid above the Coulomb threshold.

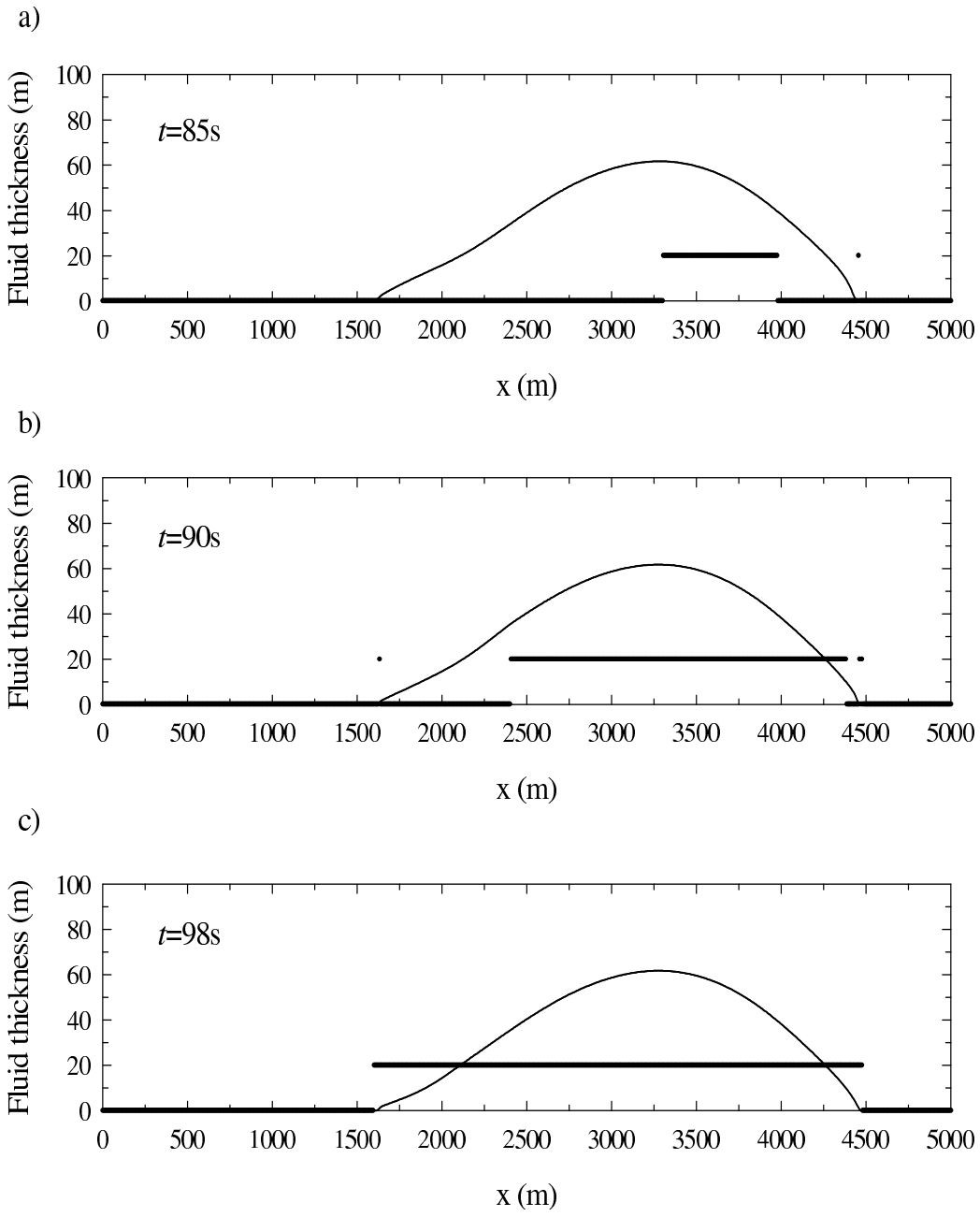

Figure 6.9: Fluid thickness (full lines) versus distance at (a) $t = 85\,s$, (b) $t = 90\,s$ and (c) $t = 98\,s$ during the stopping stage for Pouliquen's flow law with $\delta_1 = 13°$, $\delta_2 = 20°$ and $d = 1.5$. A value of 0 is allocated to the fluid under the Coulomb threshold and a value of 20 to the fluid above the Coulomb threshold.

The difference in the stopping behavior of a debris mass controlled by simple friction law or Pouliquen's flow law can be a useful test to determine the more appropriate flow law.

The presence of a fluidized zone behind a rigid mass is also observed, for example, with rheological parameters $\delta_1 = 12°$, $\delta_2 = 20°$ and $d = 10$, suggesting the existence of horizontal surfaces in the deposit. Further analysis of this phenomenon requires the development of a model reproducing the equilibrium of a fluid at rest [e.g. *Perthame and Simeoni*, 2001].

7 Conclusion

Numerical modelling of debris avalanches has been presented here based on Savage and Hutter's equations. Granular avalanche behavior has been described using a Coulomb-type friction law with constant and flow variable friction angle.

The numerical model is based on a kinetic scheme. The main idea is to introduce two different descriptions of the microscopic behavior of the system, suggested by the ambivalence of the fluid-solid behavior of granular material. The resulting solver appears to be stable and preserves height positivity, contrary to several Godounov-type methods. Efficiency of this model has been tested by comparisons with analytical solution of dam-break problems. The numerical scheme remains stable in spite of the introduction of the discontinuous Coulomb criterium. Furthermore, the discretization on a finite element mesh is well suited to simulate avalanches over real complex topographies.

Preliminary 1D simulations on a simplified geometry have allowed us to test the capacity of the numerical model and to compare constant and variable angle friction laws. The shape of the deposit strongly depends on the used friction law. Pouliquen's flow law, with a friction angle depending on the height and velocity, leads to steepest front of the granular deposit with more elongating rear. Furthermore the stopping stage differs depending on the flow law. While the stopping propagates from the front to the rear when a constant friction angle is used, the inner part of the mass begins to stop when Pouliquen's flow law is used. This feature may be a useful tool to determine the best fitted flow law when comparing with experimental results. In these oversimplified numerical tests, Pouliquen's friction law appears to be more appropriate to describe debris avalanches than a simple Coulomb friction law, suggesting that frictional effects may play a significant role in debris avalanche mechanics.
Numerical modelling of debris avalanches provides the only way to estimate typical velocities and relative weight of the involved forces. The above analysis shows that the h-gradient force does not play a significant role in the examples studied here, except at the rear and front of the granular mass. The friction force begins to be a leading force only when the granular mass approaches the stopping stage.

The numerical tests show the possible existence of a fluidized zone in the deposit, under particular conditions. In such situations, part of the fluid remains over the Coulomb threshold, subjected for example to high gravity forces, and it is still blocked by the down slope deposit suggesting the existence of horizontal zones in the deposit. Observation of such

features in real or experimental deposits would be interesting and may provide information on the mechanical behavior of a granular mass.

Acknowledgments

This work was supported by the Actions Concertées Incitatives (CNRS) "Ecoulements gravitaires" et "Modélisation de processus hydrauliques à surface libre en présence de singularités".

References

[1] Aranson, I.S., Tsimring, L.S., *Phys. Rev. E*, **64**, 020301 (R), 2001

[2] Arattano, M., Savage, W.Z., Modelling debris flows as kinematic waves, *Bull. Int. Assoc. Eng. Geol.*, **49**, 3-13, 1994

[3] Assier-Rzadkiewicz, S., Heinrich, P., Sabatier, P.C., Savoye, B., Bourillet, J.F., Numerical Modelling of a Landslide-generated Tsunami: The 1979 Nice Event, *Pure Appl. Geophys.*, **157**, 1707-1727, 2000

[4] Audusse, E., Bristeau, M.O., Perthame, B., Kinetic Schemes for Saint-Venant Equations with Source Terms on Unstructured Grids, *INRIA Report*, **3989**, 2000

[5] Azanza, E., Ecoulements granulaires bidimensionnels sur un plan incliné, *PhD of École Nationale des Ponts et Chaussées*, 1998

[6] Botchorishvili, R., Perthame, B., Vasseur, A., Equilibrium Schemes for Scalar Conservation Laws with Stiff Sources, *INRIA Report*, **8931**, 2000

[7] Bristeau, M.O., Coussin, B., Boundary Conditions for the Shallow Water Equations solved by Kinetic Schemes, *INRIA Report*, **4282**, 2001

[8] Cheng-Lun, S., Chyan-Deng, J., Yuan-Fan, T., A Numerical Simulation of Debris Flow and Its Application, *Natural Hazards*, **13**, 39-54, 1996

[9] Denlinger, R.P., Iverson, R.M., Flow of variably fluidized granular masses across three-dimensional terrain 2. Numerical predictions and experimental tests, *J. Geophys. Res.*, **106**(B1), 553-566, 2001

[10] Douady, S., Andreotti, B., Daerr, A., On granular surface flow equations, *Eur. Phys. J. B.*, **11**, 131-142, 1999

[11] Eglit, E.M., Some mathematical models of snow avalanches, *Advances in the Mechanics and the Flow of Granular Materials*, M. Shahinpoor editor, **2**, 1983

[12] Gray, J.M.N.T., Wieland, M., Hutter, K., Gravity driven free surface flow of granular avalanches over complex basal topography, *Proc. Roy. Soc. Lond. A*, **455**, 1841-1874, 1999

[13] Greve, R., Hutter, K., Motion of a granular avalanche in a convex and concave chute: experiments and theoretical predictions *Proc. Roy. Soc. Lond. A*, **342**, 573-600, 1993

[14] Greve, R., Koch, T., Hutter, K., Unconfined flow of granular avalanches along a partly curved surface. I. Theory, *Proc. Roy. Soc. Lond. A*, **445**, 399-413, 1994

[15] Harbitz, C.B., Snow Avalanche Modelling, Mapping, and Warnig in Europe, *Report of the Fourth European Framework Programme Environment and Climate*, 1998

[16] Heinrich, Ph., Boudon, G., Komorowvski, J.C., Sparks, R.S.J., Herd, R., Voight, B., Numerical simulation of the December 1997 debris avalanche in Montserrat, Lesser Antilles, *Geophys. Lett.*, **13**, 2529-2532, 2001

[17] Hunt, B., Asymptotic Solution for Dam-Break Problem, *J. Hydraul. Eng.*, **110**(8), 1985

[18] Hunt, B., Newtonian fluid mechanics treatment of debris flows and avalanches, *J. Hydraul. Eng.*, **120**, 1350-1363, 1994

[19] Hutter, K., Koch, T., Pluss, C., Savage, S.B., The dynamics of avalanches of granular materials from initiation to runout. Part II. Experiments, *Acta Mech.*, **109**, 127-165, 1995

[20] Iverson, R.M., The physics of debris flows, *Rev. Geophys.*, **35**(3), 1997

[21] Iverson, R.M., Denlinger, R.P., Flow of variably fluidized granular masses across three-dimensional terrain, 1. Coulomb mixture theory, *J. Geophys. Res.*, **106**(B1), 537-552, 2001

[22] Jenkins, J.T., Askari, E., Hydraulic theory for a debris flow supported on a collisional shear layer, *CHAOS* **9**, 654-658, 1999

[23] Laigle, D., Coussot, Ph., Numerical Modeling of Mudflows, *J. Hydraul. Eng.*, **123**(7), 617-623, 1997

[24] Macedonio, G., Pareschi, M.T., Numerical simulation of some lahars from Mount St. Helens, *J. Volcanol. Geotherm. Res.*, **54**, 65-80, 1992

[25] Mangeney, A., Heinrich, Ph., Roche, R., Analytical Solution for Testing Debris Avalanche Numerical Models, *Pure Appl. Geophys.*, **157**, 1081-1096, 2000

[26] Naaim, M., Vial, S., Couture, R., Saint-Venant approach for rock avalanches modelling, *Saint Venant Symposium*, Paris, August 1997

[27] Naaim, M., Gurer, I., Two-phase Numerical Model of Powder Avalan-che Theory and Application, *Natural Hazards*, **117**, 129-145, 1998

[28] Perthame, B., Simeoni, C., A kinetic scheme for the Saint-Venant system with a source term, *Calcolo*, **38(4)**, 201-231, 2001

[29] Perthame, B., Kinetic formulation of conservation laws, *Oxford Univ. Press*, 2002, to appear

[30] Pouliquen, O., Scaling laws in granular flows down rough inclined planes, *Phys. Fluids*, **11**(3), 542-548, 1999

[31] Pouliquen, O., Forterre, Y., Friction law for dense granular flows: application to the motion of a mass down a rough inclined plane, *J. Fluid Mech.*, **453**, 133-151, 2002

[32] Sabot, F., Naaim, M., Granada, F., Surinach, E., Planet, P., Furdada, G., Study of avalanche dynamics by seismic methods, image-processing techniques and numerical models, *Ann. Glaciol.*, **26**, 319-323, 1998

[33] Savage, S. B., Hutter, K., The motion of a finite mass of granular material down a rough incline, *J. Fluid Mech.*, **199**, 177-215, 1989

[34] Savage, S.B., Hutter, K., The dynamics of avalanches of granular materials from initiation to runout. Part I: Analysis, *Acta Mech.*, **86**, 201-223, 1991

[35] Sparks, R.S.J. et al., Generation of a debris avalanche and violent pyroclastic density current: the Boxing Day eruption of 26 December 1997 at the Soufriere Hills Volcano, Montserrat, *Geological Society Memoir*, 2001

[36] Tai, Y.C., Dynamics of Granular Avalanches and their Simulations with Shock-Capturing and Front-Tracking Numerical Schemes. PhD of Technische Universität of Darmstadt, 2000

[37] Tai, Y.C., Noelle, S., Gray, J.M.N.T., Hutter, K., Shock-Capturing and Front-Tracking Methods for Granular Avalanches, *J. Comp. Phys.*, 2002, to appear

[38] Toro, E.F., *Riemann Solvers and Numerical Methods for Fluid Dynamics*, 492 pp., Springer-Verlag, New York, 1997

[39] Whipple, K.X., Open-Channel Flow of Bingham Fluids: Applications in Debris-Flow Research, *J. Geol.*, **105**, 243-262, 1997

[40] Wieland, M., Gray, J.M.N.T., Hutter, K., Channelized free surface flow of cohesionless granular avalanches in a chute with shallow lateral curvature, *J. Fluid Mech.*, **392**, 73-100, 1999

[41] Zwinger, T., Dynamik einer Trockenscheelawine auf beliebig geformten Berghängen, PhD of the Technischen Universität Wien, 2000

Unit de recherche INRIA Rocquencourt
Domaine de Voluceau - Rocquencourt - BP 105 - 78153 Le Chesnay Cedex (France)

Unit de recherche INRIA Futurs : Domaine de Voluceau - Rocquencourt - BP 105 - 78153 Le Chesnay Cedex (France)
Unit de recherche INRIA Lorraine : LORIA, Technople de Nancy-Brabois - Campus scientiøque
615, rue du Jardin Botanique - BP 101 - 54602 Villers-ls-Nancy Cedex (France)
Unit de recherche INRIA Rennes : IRISA, Campus universitaire de Beaulieu - 35042 Rennes Cedex (France)
Unit de recherche INRIA Rhne-Alpes : 655, avenue de l'Europe - 38330 Montbonnot-St-Martin (France)
Unit de recherche INRIA Sophia Antipolis : 2004, route des Lucioles - BP 93 - 06902 Sophia Antipolis Cedex (France)

diteur
INRIA - Domaine de Voluceau - Rocquencourt, BP 105 - 78153 Le Chesnay Cedex (France)
http://www.inria.fr
ISSN 0249-6399